FOLDS ABOVE ANGULAR FAULT BENDS: MECHANICAL CONSTRAINTS FOR BACKLIMB TRISHEAR KINEMATIC MODELS

A Thesis

by

LI ZHANG

Submitted to the Office of Graduate Studies of
Texas A&M University
in partial fulfillment of the requirements for the degree of

MASTER OF SCIENCE

August 2003

Major Subject: Geology

FOLDS ABOVE ANGULAR FAULT BENDS: MECHANICAL CONSTRAINTS FOR BACKLIMB TRISHEAR KINEMATIC MODELS

A Thesis

by

LI ZHANG

Submitted to Texas A&M University
in partial fulfillment of the requirements
for the degree of

MASTER OF SCIENCE

Approved as to style and content by:

Judith S. Chester (Chair of Committee)	Frederick M. Chester (Member)
Charles P. Aubeny (Member)	Andrew Hajash Jr. (Head of Department)

August 2003

Major Subject: Geology

ABSTRACT

Folds above Angular Fault Bends: Mechanical Constraints for Backlimb Trishear Kinematic Models. (August 2003)

Li Zhang, B.E.; M.S., Southwest Petroleum Institute, P.R.China

Chair of Advisory Committee: Dr. Judith S. Chester

The backlimb trishear velocity field is compared to that of mechanical models of fault-bend folds in an incompressible anisotropic viscous media to determine the relationship between the magnitude and orientation of mechanical anisotropy and the kinematic parameters of the trishear model. The trishear model can describe the velocity field of the mechanical model, at least to first order approximation for some cases. We find that the apical angle, asymmetry angle and overall geometry of the hanging-wall syncline above the ramp depend on the magnitude and orientation of the planar anisotropy inherent in stratigraphic sequences. The asymmetry of trishear zone in the backlimb region mimics that of the planar anisotropy. In general, as the magnitude and inclination of the anisotropy increase, the trishear apical angle decreases. The trishear parameters that describe physical models of fault-bend folds with different magnitudes of anisotropy also show a decrease in apical angle with an increase in magnitude of anisotropy. Yet the apical angles of the backlimb of physical models generally are less than these predicted by the mechanical model for the same magnitude of anisotropy. In addition, the physical models display significantly more negative asymmetry than predicted by the mechanical model. The results of this study may be used to determine the conditions under which the trishear model is an acceptable approximation to natural formation and help guide the selection of trishear parameters for subsurface structural interpretations in fault-fold terrains.

To my parents and family

ACKNOWLEDGMENTS

I would like to thank the members of my advisory committee, Drs. Judith Chester, Frederick Chester, and Charles Aubeny for their advice, and guidance through the course of this study. I particularly want to thank the chairman of my committee, Dr. Judith Chester, for her help, encouragement and understanding. I have learned a lot from her about how to do scientific research and what are crucial problems for a particular research topic.

I must also thank Dr. Rick Allmendinger and Dr. Ernesto Cristallini for answering my questions in emails. Especially, I want to thank Dr. Cristallini for kindly providing the following software:

- CRISTALLINI, E.O. 2002-2003. PLIEGUES 2D©. Balance cross-sections software. CONICET-UNIVERSIDAD DE BUENOS AIRES, ARGENTINA.
- CRISTALLINI, E.O. 2000-2001. TRISHEAR 2D©. Trishear application software. CONICET-UNIVERSIDAD DE BUENOS AIRES, ARGENTINA.

I would like to thank all of the students of the Center for Tectonophysics. You guys have always offered me a helping hand whenever I needed it. Special thanks go to Elizabeth and James Slone for kindly helping me with the corrections of the thesis draft.

I would like to thank my family. I would have never finished my study without your love, and encouragement. I have lost my way a few times, but you are always the wind beneath my wings. Particularly, I would like to thank my husband Zixiang Xiong for his love and patience. Thank you for supporting me technically and mentally through all these times.

TABLE OF CONTENTS

Page

CHAPTER Page

CHAPTER Page

LIST OF FIGURES

FIGURE Page

FIGURE Page

FIGURE Page

FIGURE Page

FIGURE Page

FIGURE Page

LIST OF TABLES

CHAPTER I

INTRODUCTION

The association between faulting and folding in fold-thrust belts is generally described in terms of fault-bend folding, fault-propagation folding, and detachment folding models (Suppe, 1983; Jamison, 1987; Mitra, 1990; Suppe and Medwedeff, 1990; Chester et al. 1991).

Over the past two decades, geometric and kinematic models have been developed to describe the geometry of natural fault-fold structures and to aid in construction of balanced subsurface interpretations. Geometric models assume plane strain, conservation of cross-sectional area, and parallel kink-fold geometries (e.g., Suppe, 1983; Suppe and Medwedeff, 1990). Kinematic models often assume plain strain and a particular velocity distribution to describe hanging-wall movement. Recent kinematic models define a triangular zone of distributed shear (i.e., the trishear region) to generate smooth and rounded fold forms above angular fault bends and tips of propagating faults (e.g., Erslev, 1991; Hardy and Ford, 1997; Zehnder and Allmendinger, 2000; Johnson and Johnson, 2002a; Cristallini and Allmendinger, 2002). Trishear velocity models have been developed for fault-propagation folds (Erslev, 1991; Zehnder and Allmendinger, 2000), detachment folds (Hardy and Ford, 1997), and fault-bend folds (Cristallini and Allmendinger, 2002).

The incorporation of a trishear region to the backlimb portion of a fault-bend fold by Cristallini and Allmendinger (2002) is based on assumptions described by Zehnder and Allmendinger (2000). Within the backlimb region, the apex of the triangular zone is located above the lower angular flat-ramp corner of the fault. The backlimb trishear model generates a rounded fold form within the hanging-wall above the fault-bend, consistent with observations of natural backlimb regions of thrust sheets (e.g., Serra,1977) and analogue models of fault-bend folds (e.g., Morse, 1977; Chester et al., 1991). Although useful for subsurface interpretations where data are limited, these models allow an infinite number of velocity distributions and generate non-

---

This thesis follows the style and format of Journal of Structural Geology.

unique solutions to fold-fault form (e.g., Zehnder and Allmendinger, 2000; Johnson and Johnson, 2002b; Cristallini and Allmendinger, 2002; Cardozo et al., 2003).

Missing from the kinematic models is a direct link to material properties. Johnson and Johnson (2002a) derive a mechanical model of a forced-fold and compare the velocity solutions to those assumed for fault-propagation folds (e.g., Erslev, 1991; Hardy and Ford, 1997; Zehnder and Allmendinger, 2000). They found that under certain conditions, the mechanical model predicts a forced-fold similar to that described by the trishear models.

To date, no study has compared existing theoretical models of fault-related folds (e.g., Berger and Johnson, 1980; Kilsdonk and Fletcher, 1989; Chester and Fletcher, 1997) to the corresponding trishear model of the backlimb region (Cristallini and Allmendinger, 2002). The main goals of this study are to: (1) compare the theoretical model for a fault-bend fold of Chester and Fletcher (1997) to the recent backlimb trishear kinematic model of Cristallini and Allmendinger(2002) to determine the relationship between the specified mechanical properties and backlimb trishear parameters; (2) test the relationship with physical models of fault-bend folding (e.g., Morse, 1977; Chester, 1985; Chester et al., 1991) using information on the mechanical properties of the model components (Chester et al., 1991); (3) analyze published natural fault-bend folds, utilizing these relationships to predict the degree of anisotropy of natural sedimentary rock packages. The results of this study should help us determine the conditions under which the trishear model is an acceptable approximation of the deformation and select trishear parameters for subsurface structural interpretations in fault-fold terrains.

CHAPTER II

PREVIOUS WORK

2.1 Trishear and backlimb trishear models

2.1.1 Trishear models for fault-propagation folding

The trishear kinematic model method (e.g., Erslev, 1991) is recognized as a viable alternative to previous models that employed parallel, kink-like fold geometries (e.g., Cristallini and Allmendinger, 2002; Cardozo et al., 2003; Finch et al., 2003). The trishear method uses strain-compatibility relationships to link the concentrated simple shear, characteristic of narrow fault zones, with the distributed deformation of fault-propagation folds (e.g., Allmendinger, 1998), detachment folds (e.g., Hardy and Ford, 1997), and fault-bend folds (e.g., Cristallini and Allmendinger, 2002). The compatibility of trishear models of fault-propagation folds with natural, analogue, and mechanical models has been demonstrated in both compressional and extensional settings (Withjack et al., 1990; Mitra and Islam, 1994; Erslev, 1991; Johnson and Johnson, 2002a). Footwall synclines commonly observed in nature, but not well described in many earlier kinematic models, are produced both in 2-D and 3-D trishear fault-propagation folding simulations (Erslev, 1991; Hardy and Ford 1997; Allmendinger 1998; Cristallini and Allmendinger, 2001).

Zehnder and Allmendinger (2000) present a precise and simple method to derive a velocity solution for trishear deformation assuming incompressible flow. Zehnder and Allmendinger (2000) simulate deformation through numerical integration using linear and non-linear velocity fields. This approach leads to an infinite number of potential velocity fields and allows for variations in fold geometry given the different velocity descriptions. It enables the comparison between the velocity fields predicted by trishear-like mechanical models (e.g., Johnson and Johnson, 2002a) to the kinematic model.

2.1.2 Backlimb trishear model

Models assuming kink-like parallel folding do not replicate curved fold surfaces and complex strain patterns documented for natural and experimental faults. Cristallini and Allmendinger (2002) present a backlimb trishear kinematic model to describe the distributed deformation in a backlimb of a fault-bend structure above an angular bend in an underlying fault surface. Different from the original trishear kinematic model of Erslev (1991), the backlimb trishear zone develops at the lower ramp-flat corner of a fault-bend fold. The deformation is constrained inside a triangular zone above the lower fault bend. Backlimb trishear explains the rounded fold form generated above the angular fault bend by progressive bed rotation within the triangular zone.

Cristallini and Allmendinger (2002) present a linear velocity solution for the velocity in the triangular trishear zone (Fig. 2.1, Appendix B). The axes $x' - y'$ represent the local coordinate system, where x' is the bisector of the trishear zone, y' is perpendicular to x' in the counter-clockwise direction. The global coordinate system is represented by $x - y$, where y is directed downward. Conservation of area within the triangular zone and incompressibility are assumed. The material above the lower flat moves as a rigid block parallel to the lower flat at a velocity V_0, while the material above the ramp moves at a velocity V_1.

The trishear geometry is described by two parameters. The apical angle (2φ, Fig. 2.1) characterizes the opening of the triangular zone and bed thickness changes (Cristallini and Allmendinger, 2002). The zone of shear is more focused for smaller apical angles and the backlimb trishear model is identical to the kink-band model of a fault-bend fold (Suppe, 1983) for $2\varphi = 0$. The asymmetry angle, α_{ca}, is the angle between the bisector of the fault bend and bisector of the backlimb trishear apical angle (Fig. 2.1c). The trishear zone is symmetric for $\alpha_{ca} = 0$ and $V_0 = V_1$. The asymmetry is defined as positive when $V_0 < V_1$ and the triangular zone leans towards the foreland. Negative asymmetry occurs when $V_0 > V_1$ and the backlimb is inclined towards the hinterland. Asymmetry greatly affects the resulting fold geometry; positive asymmetry will result in thinning in the hanging-wall syncline and in the backlimb. Negative asymmetry will result in thickening in the hanging-wall syncline and in the backlimb.

The backlimb trishear kinematic model has been compared to physical models of fault-bend folds (Morse, 1977; Chester et al., 1991) by comparing the strain distribution and fold geometry (Cristallini and Allmendinger, 2002). Cristallini and

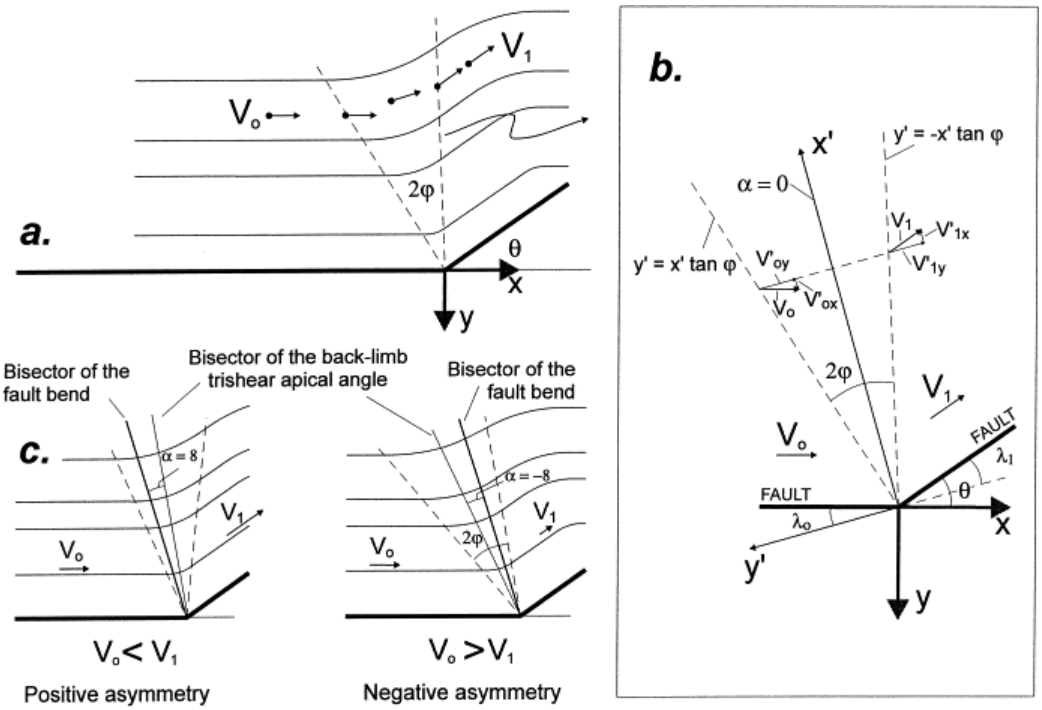

Fig. 2.1. The geometry and parameters defined in backlimb trishear model. (a) Velocities are uniform and parallel to fault segments outside of the trishear zone. Backlimb trishear assumes that materials rotate within trishear region. (b) Coordinate systems and the angle relations. B represents the bisector of the fault bend. It matches with x' only when $\alpha_{ca} = 0$. (c) The asymmetry angle α_{ca} is defined to be the angle between x' and backlimb bisector. Dash lines represent the boundaries of trishear zone. Modified from Cristallini and Allmendinger (2002).

Allmendinger (2002) suggest that if fractures are generated under shear and extension within a backlimb triangular zone, and if the fractures are subjected to progressive rotation and translation up the ramp, the backlimb trishear model matches well with physical models. Their hypothesis and predicted failure patterns are consistent with the fracture fabric of physical models (e.g., Chester et al. 1991).

2.2 Mechanical models of fault-bend folds

Rich (1934) suggested that large folds in thrust sheets develop as passive folds during the translation of hanging walls over ramp segments of faults. Since then, several analytical models have been developed to understand the geometry, kinematics, and mechanics of thrust sheet evolution (e.g., Wiltschko, 1979a, b; Berger and Johnson, 1980, 1982, Kilsdonk and Fletcher, 1989; Johnson and Fletcher, 1994; Chester and Fletcher, 1997; Johnson and Johnson, 2002b).

Mechanical modeling of stress and deformation associated with movement on a frictionless fault has been addressed for crustal rock with both isotropic and anisotropic rock properties (Berger and Johnson, 1980, 1982; Kilsdonk and Fletcher, 1989, Chester, 1992; Chester and Fletcher, 1997). Mechanical analyses indicate that stress and deformation in the vicinity of a thrust ramp may be associated with the translation of the thrust sheet over the fault surface (Berger and Johnson, 1980, 1982; Kilsdonk and Fletcher, 1989, Chester, 1992; Chester and Fletcher, 1997). Kilsdonk and Fletcher (1989) suggest that in some cases the translation may be the dominant deformation process because strain rate due solely to sliding is typically of the same order as the regional strain rate.

Berger and Johnson (1980) model the formation of a ramp anticline assuming a linear viscous, incompressible hanging-wall sliding on a frictionless surface above a rigid footwall. Their first-order analysis (accurate to first order in the slope of interface) is valid for a moderate ramp angle (15° to 20°).

The analytical model of Kilsdonk and Fletcher (1989) investigates deformation in both the hanging-wall and footwall. They conduct a first-order analysis of two incompressible viscous half-spaces separated by a frictionless sliding surface, which is composed of multiple sinusoidal components. They illustrate that the stress and deformation in the hanging-wall are mirror images to those in the footwall. The results provide a mechanical description of footwall deformation in nature.

Chester and Fletcher (1997) model deformation of an anisotropic media in the vicinity of a bend on a frictionless fault. The analysis follows that of Berger and Johnson (1980), and extends the analysis of Kilsdonk and Fletcher (1989) by considering a planar mechanical anisotropy of variable orientation and magnitude.

The deformation process in the Chester and Fletcher (1997) model is a combination of geometric perturbation when the upper half space passes over the ramp and the mechanical effect of anisotropic material properties.

Similar to previous mechanical models (e.g., Berger and Johnson, 1980; Kilsdonk and Fletcher, 1989), the mechanical analysis of Chester and Fletcher (1997) assumes that the hanging-wall thickness is greater than the ramp width, deformation is by plane strain, no separation is allowed along the sliding surface, and deformation arises solely due to translation of incompressible material past the ramp. The strength of the sliding surface is assumed to be zero and deformable. Chester and Fletcher (1997) consider two scenarios: a simple sinusoidal sliding surface geometry, and a geometry containing a periodic array of isolated bends. The periodic array of isolated bends is mathematically represented with a truncated Fourier series, whose components are simple sinusoidal sliding surfaces. The sliding surface is an angular (locally smooth-curving) frictionless ramp joining two long flats. The length of the flat is 20 times the width of the ramp (W), so that the thrust ramps are isolated and the interference between ramps is negligible (Kilsdonk and Fletcher, 1989).

The Chester and Fletcher (1997) model assumes incompressible viscous fluid behavior. The degree of anisotropy (m) is defined to be the ratio of normal viscosity η_n and shearing viscosity η_s. The material is isotropic for $m = 1$, and anisotropic for $m > 1$.

The total deformation of the anisotropic media can be described as the linear combination of a basic flow and a perturbing flow. The basic flow is associated with sliding on the interface, which is uniformly translated at a velocity of $V/2$ (see Fig. 2.2). The perturbing flow arises due to the geometric perturbation of the sliding surface.

Combining the constitutive relations, equations of equilibrium, and the deformation rate compatibility equation, an analytical solution in the upper half-space was derived by Chester and Fletcher (1997). Because the media separated by the sliding surface is equivalent, the stress and deformation in the lower half-space are the mirror images, across the mean sliding surface, of those in the upper half-space.

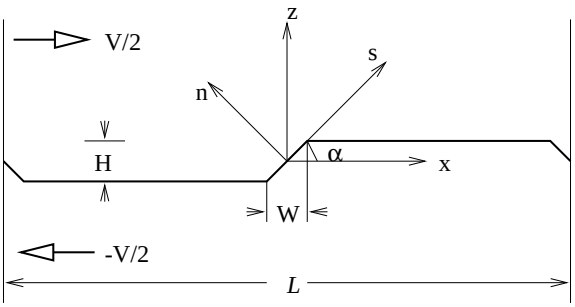

Fig. 2.2. Model geometry of a periodical array of isolated bends. The upper region and lower region slide relative to the interface at a velocity $V/2$ and $-V/2$ respectively. The axes x and z are parallel and perpendicular to the mean orientation of the sliding surface, respectively. The principal orientations of anisotropy are parallel to the local coordinate axis s and n, where n and s denote the coordinate directions perpendicular and parallel to the anisotropy plane. Redrawn from Chester and Fletcher (1997).

CHAPTER III

COMPARISON OF BACKLIMB TRISHEAR MODELS TO MECHANICAL MODELS

3.1 Velocity fields

3.1.1 Velocity field of the trishear models

3.1.1.a Velocity in the trishear region above an angular fault bend

The trishear velocity field in the backlimb region above an angular fault bend is defined by Cristallini and Allmendinger (2002), with one minor modification (see Fig. 3.1). The y direction in the global coordinate system is taken as positive upwards, rather than downward. Sign changes have been made to the equations (5) and (7) of Cristallini and Allmendinger (2002) to satisfy the incompressible flow assumption (Equations B.5 and B.7 from Appendix B).

The numerical calculation of the velocity field has two steps. First, the velocity field is calculated in the local coordinate system ($x' - y'$) using Matlab 6.0. Then, the velocity field is transformed from the local coordinate system to the global coordinate system.

The trishear velocity field of Cristallini and Allmendinger (2002) assumes a linear variation in velocity across the trishear zone and satisfies the incompressibility assumption (Equation(3.1) and Fig. 3.2). For a negative α_{ca}, there is a geometric limit set by the lower flat. In this case, the hinterland boundary of the triangular zone coincides with the lower flat. For a positive α_{ca}, the geometric limit is set by the fault ramp. So, the limit of asymmetry angle for a given geometric setting is

$$90^\circ - \frac{\theta}{2} > |\alpha_{ca}| + \varphi. \tag{3.1}$$

For example, if the fault angle is 20°, the apical angle of the trishear zone is 40° and possible asymmetry angles range from -60° to 60°.

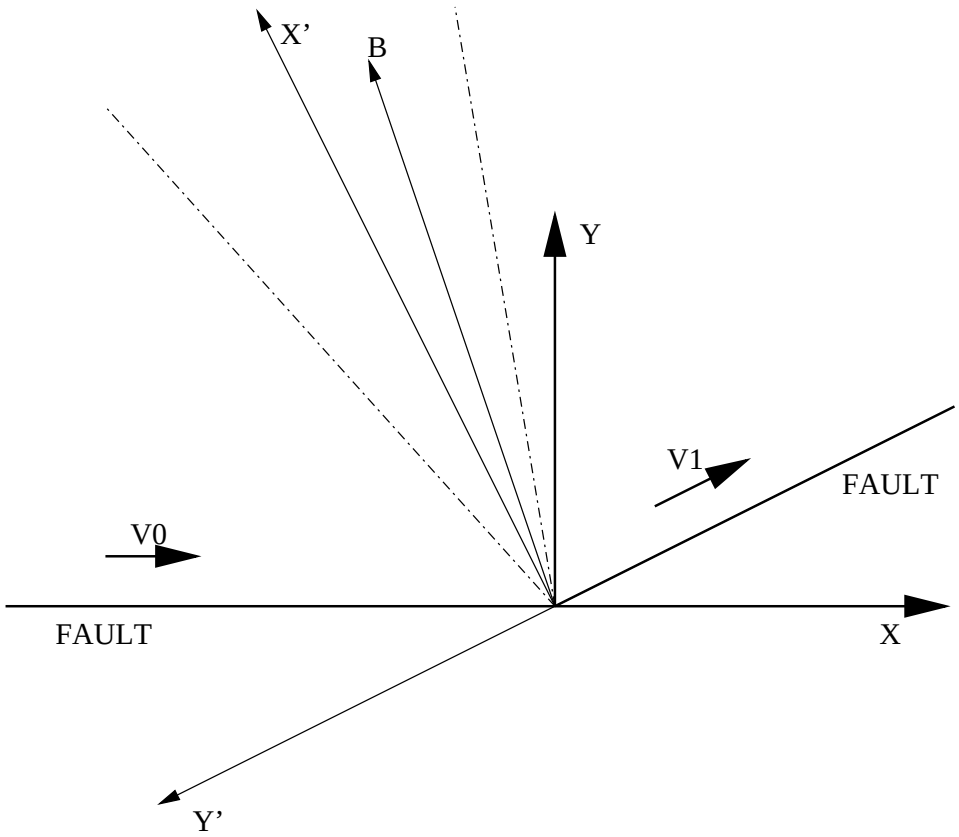

Fig. 3.1. Modified coordinate systems of backlimb trishear model. The axes $x' - y'$ represent the local coordinate system, where x' is the bisector of trishear apical angle, y' is perpendicular to x' in a counter-clockwise manner. Global coordinate system is labeled as $x - y$, where x is right-hand and y is normal to x in a counter-clockwise manner. B is the backlimb bisector. For $\alpha_{ca} = 0$, $x' = B$. Dash lines represent the boundaries of trishear zone. Redrawn from Cristallini and Allmendinger (2002).

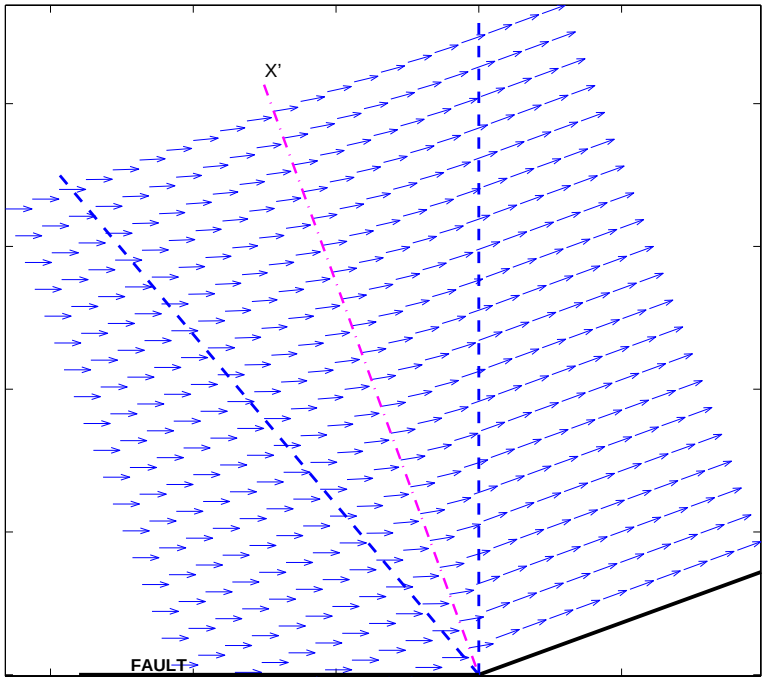

Fig. 3.2. Velocity field at the backlimb region of a fault-bend fold. The velocity solution follows backlimb trishear kinematic model of Cristallini and Allmendinger (2002). The fault angle is 20°, trishear apical angle is 40°, and the asymmetric angle of triangular zone is −10°. X' is the trishear bisector. Dash lines mark the boundaries of backlimb trishear zone.

3.1.1.b Trishear velocity model of the backlimb region of a fault-bend fold

The kinematics of the backlimb region of a fault-bend fold reflects both the upper and lower fault bends. Here we extend the model of Cristallini and Allmendinger (2002) to determine the velocity above the backlimb of a fault-bend fold by adding an additional forelimb trishear zone above the upper fault bend.

In order to derive the velocity field for the fault-bend fold, we define three coordinate systems. The local coordinate system $x'_1 - y'_1$ and the global coordinate system $x - y$ are identical to the modified coordinate systems for the isolated bend (Fig. 3.1). The forelimb trishear zone is defined by the third local coordinate system $x'_2 - y'_2$, where x'_2 is parallel to x'_1 and y'_2 is parallel to y'_1.

The two trishear zones are separated by a fault ramp with dip angle θ. Each trishear zone satisfies the assumptions given by Cristallini and Allmendinger (2002). It is assumed that velocity varies only within the two triangular zones and the area is preserved.

The material on the hanging-wall moves towards the forelimb with an initial velocity V_0. The orientation and magnitude of velocity change within the backlimb trishear zone satisfying the backlimb velocity solution derived by Cristallini and Allmendinger (2002). After exiting the backlimb trishear zone, the beds move uniformly at velocity V_1 parallel to the ramp. The beds again rotate within the forelimb trishear zone, (unfold) and upon exiting moves at a velocity of V_0 parallel to the upper flat.

To describe the forelimb trishear zone, we choose the same velocity solution as in the backlimb trishear zone. The velocity field of the trishear model is the sum of the velocities in each trishear zone. Thus, the initial conditions for each individual trishear zone have to be changed to satisfy the assumptions. The velocity upon entering the backlimb trishear zone is equal to $V_0 - V_1/2$. The velocity after exiting the first trishear zone and entering the forelimb trishear zone is $V_1/2$. After exiting the forelimb trishear zone, the velocity is $V_0 - V_1/2$.

3.1.2 Velocity field of the mechanical model

3.1.2.a Velocity field for a sinusoidal sliding surface

The elementary unit of a periodic array of isolated bends is a simple sinusoidal

sliding surface. For this reason, the velocity field and deformation above a sinusoidal sliding surface is reviewed.

The basic state flow is of constant magnitude and horizontally directed. The perturbing flow is of variable magnitude and direction, and reflects the geometric perturbation as a result of movement past a nonplanar fault surface.

The perturbing and total flow for both the isotropic and anisotropic cases are discussed in detail by Kilsdonk and Fletcher (1989) and Chester and Fletcher (1997). The perturbing flow of both cases display a cellular form in the x direction with flow moving away from a thrust ramp and towards normal ramps. The cellular lobes are extended to a greater distance and oriented parallel to the principal directions of anisotropy in anisotropic case (Fig. 3.3 and 3.4). The velocity vectors for the perturbing flow near the interface are parallel to the z direction and decrease in magnitude with distance from the sliding surface. The total flow combines the perturbed flow and basic state flow. The particle motions for the total flow mimic the wavy sliding surface and decrease in magnitude with distance from the sliding surface.

3.1.2.b Velocity field for an isolated thrust ramp

If the bends (i.e., ramps) are separated by relatively long flats and ramp-flat corners are sufficiently sharp, i.e., $N > 32$ (Chester and Fletcher, 1997), the periodic array of isolated bends represents the idealized geometry of a thrust fault having an isolated ramp between two flats as idealized by Rich (1934).

The perturbing flow velocity field for a sliding surface with isolated thrust and normal ramps is shown in Fig. 3.5. The width of the flat in this example is 20 times of ramp width, and the ramp angularity parameter is $N = 100$. Similar to the sinusoidal sliding surface case (Fig. 3.3 and 3.4), the velocity vectors diverge from the thrust ramp and converge towards the normal ramps. The velocity patterns are symmetrical across the z axis of the global coordinate system, $x-z$, for the case of isotropic media. The cellular patterns of perturbing flow in the anisotropic case are asymmetric across the z axis, and preferentially oriented to be parallel to the principal orientation of anisotropy.

The velocity distribution about an isolated thrust ramp changes with an increase in m and α (Fig. 3.5). The velocity vectors are elongated parallel to the principal directions of the anisotropy in the anisotropic case (Fig. 3.5b). With the increase

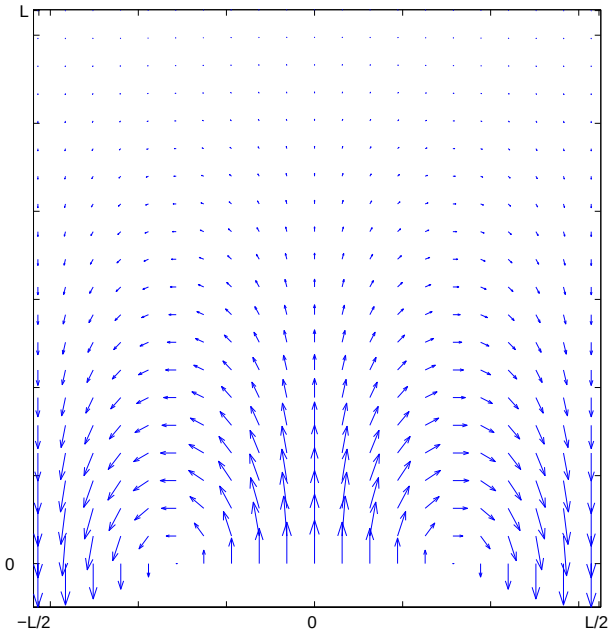

(a)

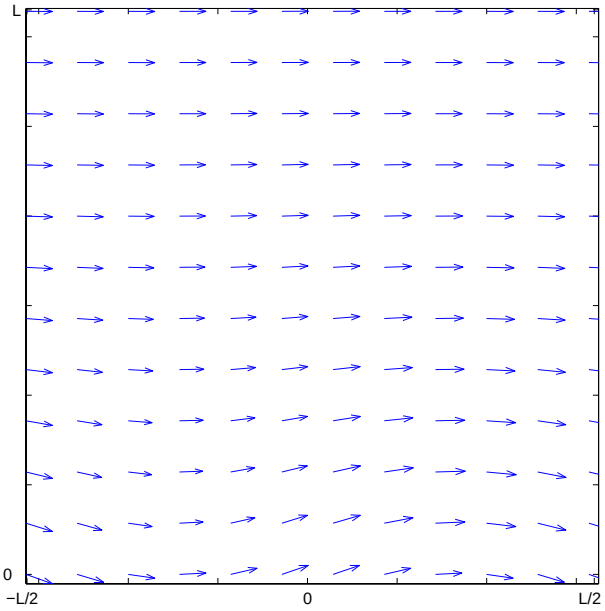

(b)

Fig. 3.3. Velocity distribution for isotropic media ($m = 1$) above a sinusoidal sliding surface. With maximum ramp dip of 10°, the sliding surface approximates a horizontal line. The mapped region of this figure is $-L/2 \leq x \leq L/2, 0 \leq z \leq L$. Basic flow is right lateral. (a) Velocity field of perturbed flow. The head of arrow is pointing to the direction of particle movement. The length of arrow represents the magnitude of velocity. (b) Total flow (the sum of basic flow and perturbed flow). It mimics the particle path.

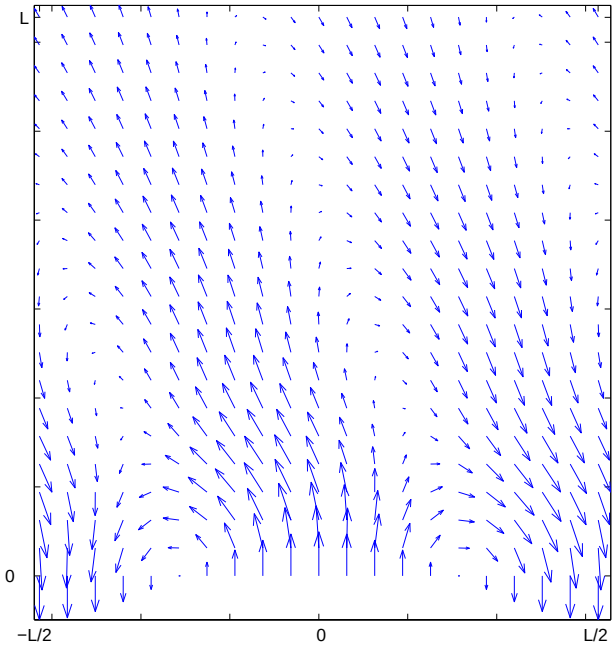

(a)

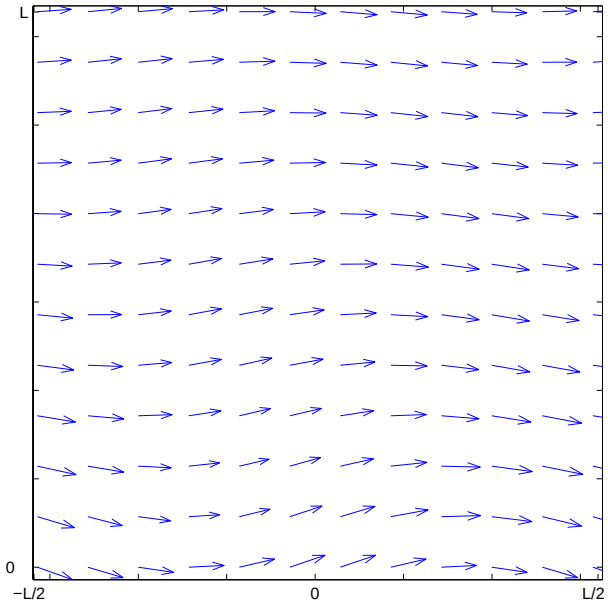

(b)

Fig. 3.4. Velocity distribution for anisotropic media ($m = 10, \alpha = 22.5°$) above a sinusoidal sliding surface. With maximum ramp dip of 10°, the sliding surface approximates a horizontal line. The mapped region of this figure is $-L/2 \leq x \leq L/2, 0 \leq z \leq L$. Basic flow is right lateral. (a) Velocity field of perturbed flow. The head of arrow is pointing to the direction of particle movement. The length of arrow represents the magnitude of velocity. (b) Total flow (the sum of basic flow and perturbed flow). With distance from the sliding surface, the particle path and sliding surface are out of phase as a result of the inclined anisotropy.

in anisotropy magnitude (m), the perturbing flow extends farther from the thrust ramp. On the basis of comparison of the magnitude of the perturbing flow generated in isotropic media to that in anisotropic media at corresponding locations, the perturbation for the anisotropic case is clearly more pronounced.

3.1.3 Comparison of trishear and mechanical model velocity fields

The gross form of the total velocity distribution as defined by the mechanical model of Chester and Fletcher (1997), for the region above the lower flat-ramp corner (Fig. 3.6a) is similar to that of the backlimb trishear kinematic model (Fig. 3.6b). First, the trishear model velocities above the lower flat are parallel to the lower flat. Velocities of the mechanical model (Fig. 3.6a) at corresponding locations also are uniformly parallel to lower flat due to the basic flow. Second, the velocities after exiting the foreland triangular boundary are parallel to the ramp but decrease in magnitude with distance from the sliding surface (Fig. 3.6a). Third, within the triangular region, the magnitude and orientation of velocity vectors change progressively. These observations match the general characteristics of the backlimb trishear model.

3.2 Fold geometry

3.2.1 Fold geometry simulated with backlimb trishear kinematics

The backlimb geometry produced using the linear velocity description presented by Cristallini and Allmendinger (2002) is shown in Fig. 3.7. Thickening or thinning of layer markers occurs in the trishear zone over the ramp and depends on the asymmetry angle. When asymmetry is zero, the thickness of layers in the backlimb are slightly thinned. Introduction of negative asymmetry will result in thickening in the hanging-wall syncline and in the backlimb (Fig. 3.7b). The thickness changes are more pronounced with larger apical and asymmetry angles (Cristallini and Allmendinger, 2002).

3.2.2 Fold geometry generated with the mechanical model

Displacement of the hanging-wall over the footwall produces geometric changes in the hanging-wall to accommodate the successive particle motion up the ramp.

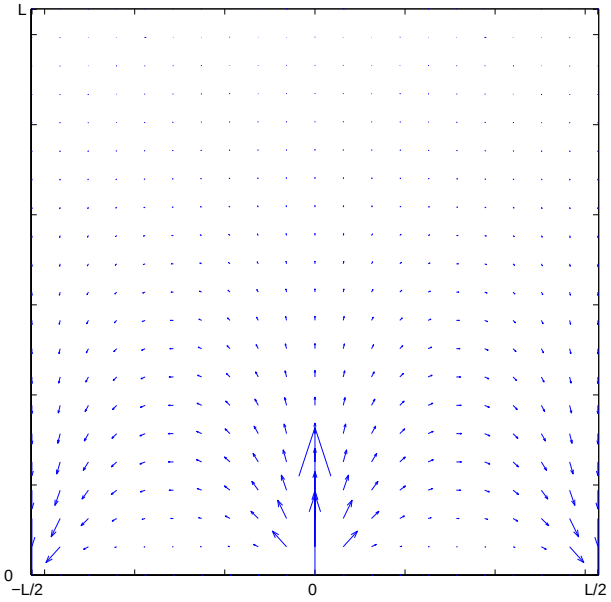

(a)

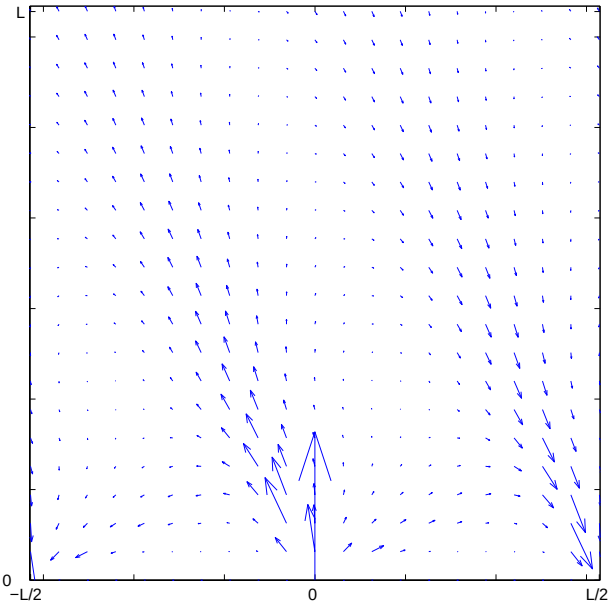

(b)

Fig. 3.5. Velocity fields of the perturbed flow above an isolated thrust ramp. The region of plots is $-L/2 \leq x \leq L/2$ and $0 \leq z \leq L$. The thrust ramp has a maximum slope of 10° and ramp angularity parameter $N = 32$. (a) The perturbed flow for the case of isotropic media ($m = 1, \alpha = 0°$). (b) The perturbed flow for anisotropic media with $m = 10$ and $\alpha = 22.5°$.

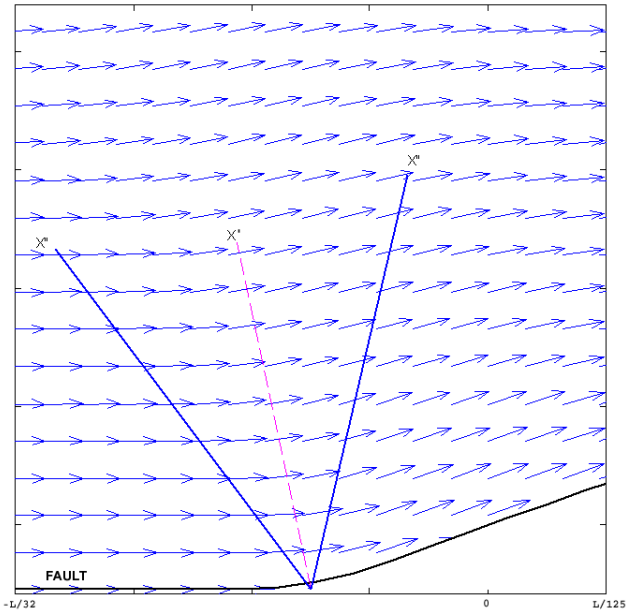

(a)

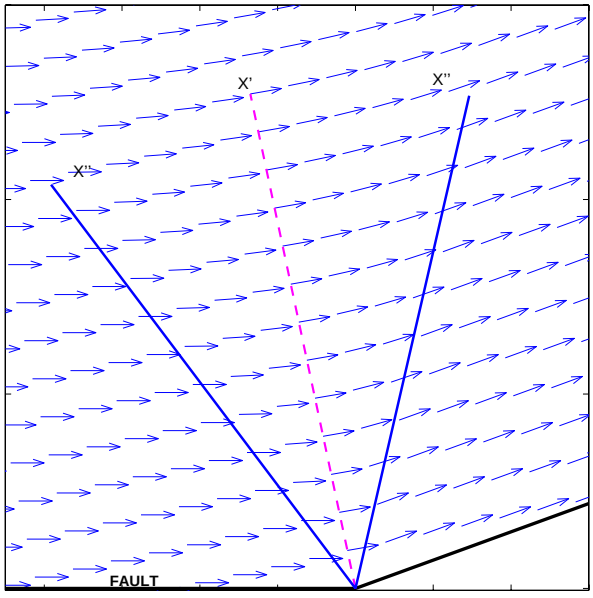

(b)

Fig. 3.6. Comparison of velocity fields at the backlimb of angular faults. X' represents the bisector of trishear zone. Solid lines (X'') represent the triangular boundaries. (a) Total velocities are solved for an isolated thrust ramp with Chester and Fletcher (1997) mechanical model. Case shown here is anisotropic ($m = 10, \alpha = 30°$). The apical angle of the triangular zone is 50°. The thrust ramp has a maximum slope of 20° and a ramp angularity parameter $N = 100$. (b) Velocities are solved with backlimb trishear kinematics. The fault angle is 20°, apical angle of trishear zone and asymmetry angle are 50° and −2°, respectively.

(a)

(b)

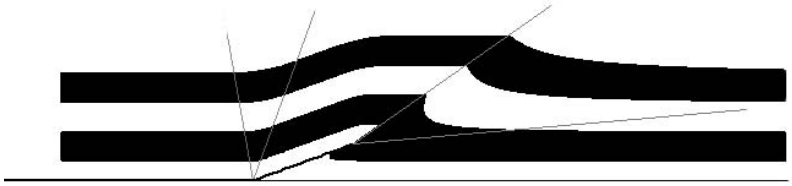

(c)

Fig. 3.7. The effect of asymmetry on the backlimb geometry of trishear fault-propagation folds. The geometries at the forelimb are calculated using Zehnder and Allmendinger (2000) trishear equations. Fault angle is 20°, and backlimb apical angle is 30°. The backlimb geometries are generated with the same backlimb trishear variables except the asymmetry angle. (a) Symmetric ($\alpha_{ca} = 0°$). (b) Asymmetric ($\alpha_{ca} = -15°$). (c) Asymmetric ($\alpha_{ca} = 15°$). Simulated with TRISHEAR 2D software of E. Cristallini (2001).

An efficient way to investigate this process is to consider and record what happens to initially orthogonal grids as a result of successive, cumulative displacements. A 61×61 orthogonal grid is superposed on the hanging-wall portion of the fault. All elements in the grid are connected by bars through nodes. Initially square grids, representing the intact media, are distorted after a small increment of sliding. The final fold form is represented by the distorted grids.

The fold forms produced using the mechanical models are generated by computing the velocity at nodes of a grid and stepping displacements of material points through time. This process is generated using a Matlab source code (See Appendix C for detailed information on the realization of deformation grids).

After 3 ramp widths of sliding above an isolated thrust ramp, a portion of the hanging-wall deforms as shown in Fig. 3.8. Material above a thrust ramp, represented with initially square grids, extends horizontally and shortens vertically. The bending of initially vertical lines can be interpreted in terms of fault drag (Kilsdonk and Fletcher, 1989). The horizontal extension in the cores of folds (Fig. 3.8 and 3.9) suggest normal drag on the forelimbs and reverse drag on the backlimbs.

The hanging-wall motion due to the joint effect of horizontal translation and geometric perturbation over the ramp forms a locally rounded fold geometry. The fold geometry is compatible with observations of analog models of thrust ramps (e.g., Morse, 1977; Chester et al., 1991), natural ramp-fold observations by Rich (1934), and broadly consistent with the results of all other fault-bend folding models (e.g., Suppe, 1983). The magnitude of the distortion of nodal points increases towards the lower fault bend. Differences in fold geometry between the isotropic and anisotropic cases are more pronounced with increasing height above the ramp. The resultant fold geometry tapers from steeper dip angles in both the forelimb and backlimb, near the fault interface to smaller dip angles at higher stratigraphic levels. At the same stratigraphic level of the deformation grids, the forelimb dip is larger in the anisotropic case than in the isotropic case.

Bed thickness changes occur in both isotropic and anisotropic cases and become more pronounced when $|\alpha|$ increases. Horizontal anisotropy ($\alpha = 0$) will result in a slightly thinned backlimb and slightly thickened forelimb (Fig. 3.10a and 3.11a). The thickening or thinning occurs in the backlimb and moves up ramp. When $\alpha < 0$, the marker horizons are thinned in the backlimb and thickened in the forelimb (Fig. 3.10b and 3.11b). When $\alpha > 0$, the marker horizons are thickened in the backlimb and

thinned in the forelimb (Fig. 3.10c and 3.11c). The incompressible flow condition, as assumed by the mechanical models, ensures that cross-sectional area is conserved. Thus, the amplitude of the fold crest in each case is constant.

Table 3.1. Deformation grids matrix.

N	m	α	Maximum slope	Displacement	Figure Number
100	1	0°	20	$3W$	3.8
32	10	0°	20	$3W$	3.10a
32	10	−22.5°	20	$3W$	3.10b
32	10	22.5°	20	$3W$	3.10c
100	10	0°	20	$3W$	3.11a
100	10	22.5°	20	$3W$	3.9, 3.11b
100	10	−22.5°	20	$3W$	3.11c

Increasing the number of terms of Fourier series (N) will result in sharper ramp-flat corners (Chester, 1992). As a ramp corner sharpens, the resultant fold geometry becomes more angular with well-defined hinges (Fig. 3.10 and 3.11). Increasing N produces kink-like folds that are similar to the fault-bend fold geometry of Suppe (1983).

3.2.3 Comparison of trishear and mechanical model fold geometries

The backlimb trishear kinematic model presents a velocity solution that is only valid at the backlimb region of a fault-bend fold, and thus are only able to produce the backlimb geometry of a fault-bend fold. Accordingly, the following compares the backlimb geometry of the backlimb trishear model with the backlimb of the mechanical model.

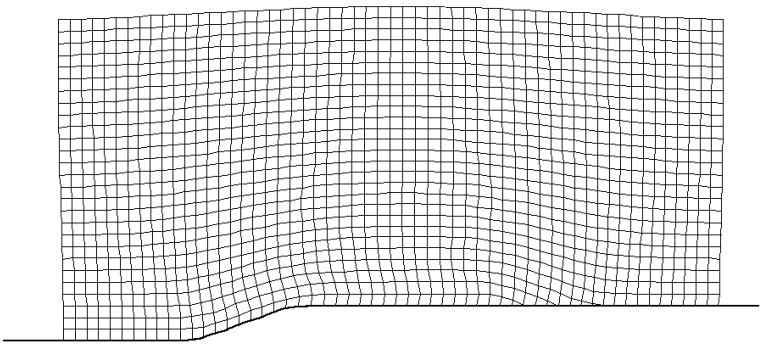

Fig. 3.8. Deformed grids illustrating the hanging-wall distortion as a result of total flow on an isolated thrust ramp for isotropic case ($m = 1, \alpha = 0°$). The thrust ramp has a maximum slope of 20° and ramp angularity parameter $N = 100$. The total displacement is accumulated over 20 iterations with a total displacement of 3 ramp widths.

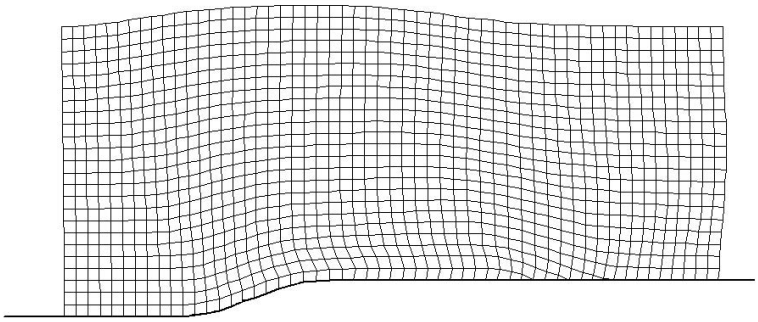

Fig. 3.9. Deformed grids illustrating the hanging-wall distortion as a result of total flow on an isolated thrust ramp for anisotropic case ($m = 10, \alpha = 22.5°$). The thrust ramp has a maximum slope of 20° and ramp angularity parameter $N = 100$. The total displacement is accumulated over 20 iterations with a total displacement of 3 ramp widths.

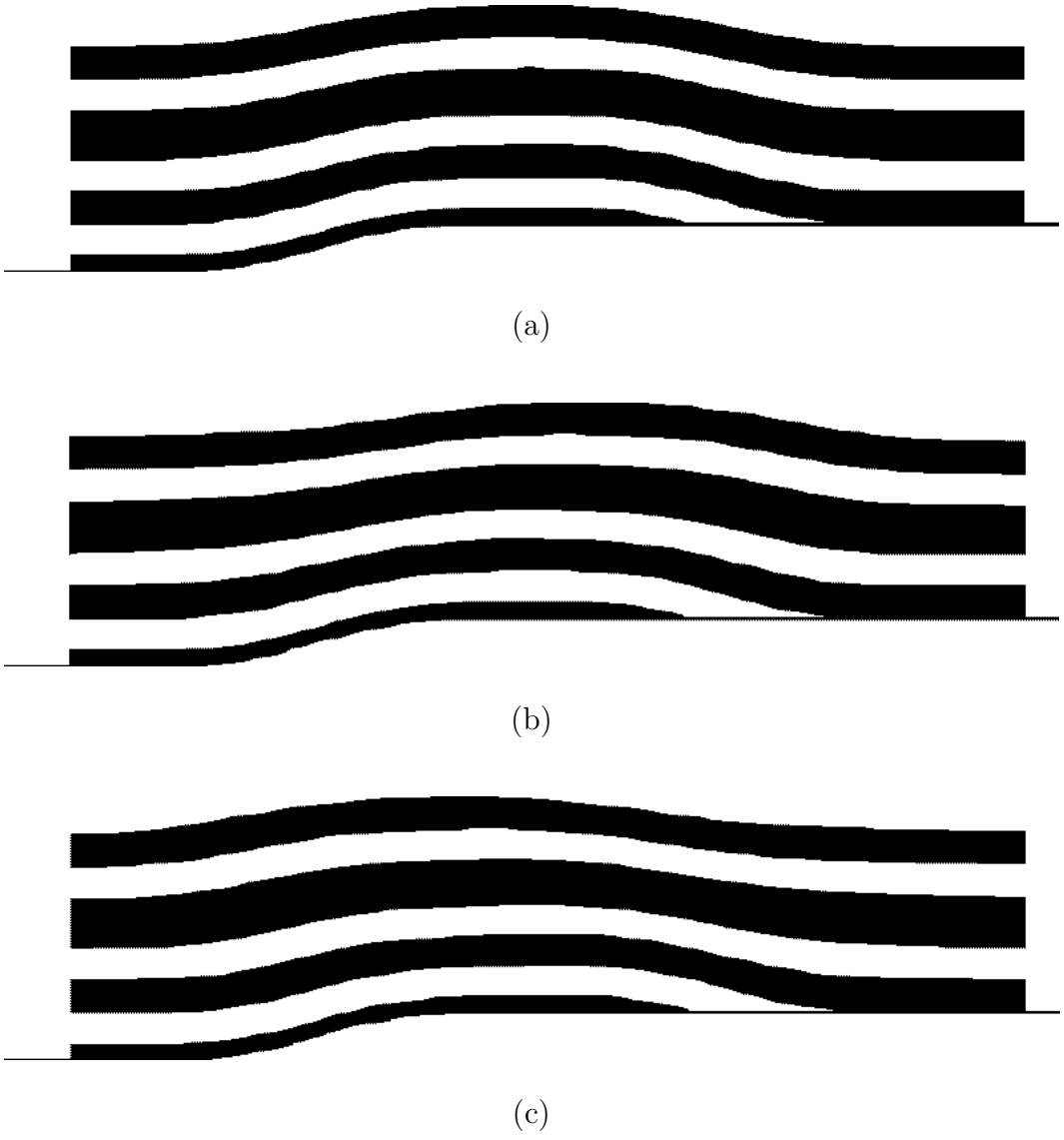

(a)

(b)

(c)

Fig. 3.10. The effect of asymmetry on the fold geometry. The fold geometry is simulated with the deformation grids of the Chester and Fletcher (1997) mechanical model. The thrust ramp has a maximum slope of 20° and ramp angularity parameter $N = 32$. The total displacement is accumulated over 20 iterations with a total displacement of 3 ramp widths. The cases shown are anisotropic ($m = 10$). (a) $\alpha = 0°$. (b) $\alpha = -22.5°$. (c) $\alpha = 22.5°$.

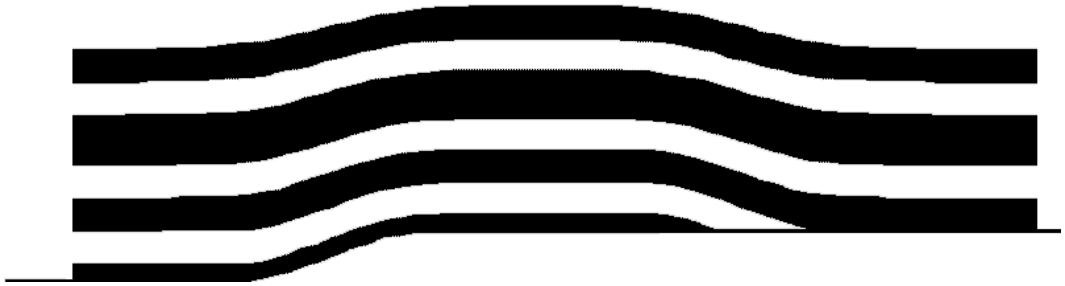

(a)

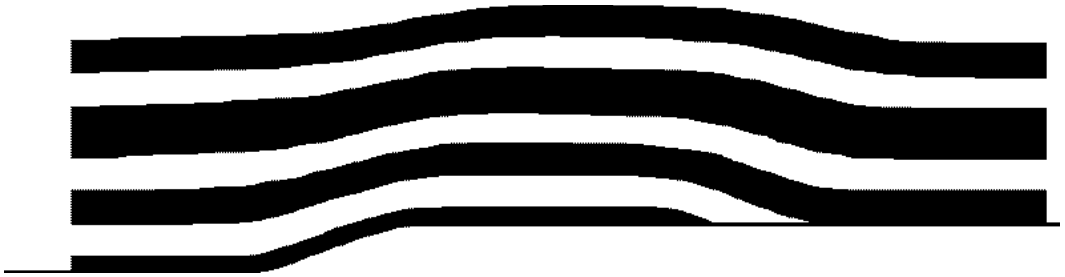

(b)

(c)

Fig. 3.11. The effect of asymmetry on the fold geometry. The fold geometry is simulated with the deformation grids of the Chester and Fletcher (1997) mechanical model. The thrust ramp has a maximum slope of 20° and ramp angularity parameter $N = 100$. The total displacement is accumulated over 20 iterations with a total displacement of 3 ramp widths. The cases shown are anisotropic ($m = 10$). (a) $\alpha = 0°$. (b) $\alpha = -22.5°$. (c) $\alpha = 22.5°$.

The backlimb regions for the anisotropic cases are rounded, consistent with the rounded backlimb geometry of the trishear model (Fig. 3.7). After 3 ramp widths of displacement, the mechanical model produces a flat-crested fold. The simulations of fold geometry in the backlimb trishear model all contain flat crests.

Bed thickness changes occur in both the backlimb trishear and mechanical models. By changing trishear asymmetry angles, backlimb trishear kinematics produce three different bedding thickness variations. The mechanical model is able to produce the three cases with corresponding thickness change patterns (Fig. 3.10 and 3.11).

A triangular region of concentrated deformation can be roughly placed at the backlimb region of the mechanical model. It is likely that we can approximate the mechanical model with a triangular zone in the backlimb.

CHAPTER IV

CORRELATION OF MECHANICAL PARAMETERS AND BACKLIMB TRISHEAR PARAMETERS

The velocity fields of the trishear models and mechanical models are compared using velocity contour plots to determine the relationship of the kinematic parameters (α_{ca} and 2φ) and mechanical parameters (m and α).

4.1 Reference Velocity and β contour plot

Cristallini and Allmendinger (2002) assume that V_0 and V_1 are constant and parallel to the flat and ramp, respectively. Because the velocity distribution in the backlimb region of the model is symmetric across the trishear bisector, the velocity at the trishear bisector is a constant and equal to $(V_0 + V_1)/2$.

To facilitate the comparison of the velocity distribution in the mechanical models to that in the backlimb trishear model, we define a reference velocity, V_R, as:

$$V_R = (V_{flat} + V_{ramp})/2 \tag{4.1}$$

where V_{flat} is the velocity of hanging-wall particle on the lower flat of a fault-bend fold, and V_{ramp} is the velocity on the ramp. In the trishear model, V_{flat} equals V_0, V_{ramp} equals V_1, and the reference velocity is equal to $(V_0 + V_1)/2$.

The velocity fields of the trishear and mechanical models may be compared using plots that contour the angular deviation of the velocity relative to the reference velocity. The dot products of velocity vectors, V, and reference velocity reveal the angular relationship between V and V_R, defined as β. As the velocity along the trishear bisector is defined to be V_R, the $\beta = 0^\circ$ contour line corresponds to the trishear bisector. β is positive if the vector V is counter-clockwise away from V_R. Each β contour is based on a 81×81 grid.

4.1.1 β contour plot for trishear models

Fig. 4.1 is a β contour plot for an isolated trishear zone above a fault-bend

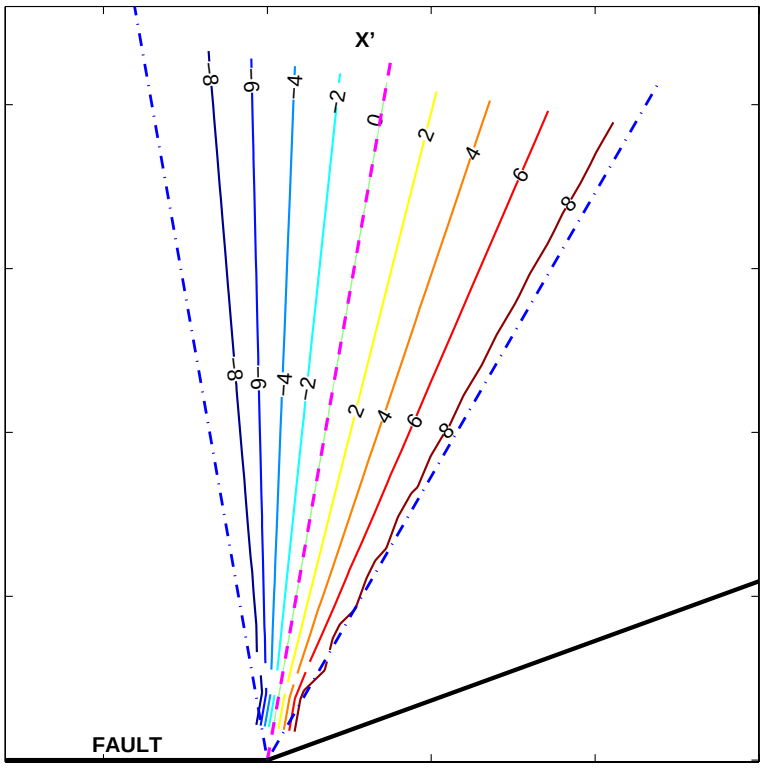

Fig. 4.1. Contour plot of the deviations of velocity from reference velocity for trishear model. The fault angle is 20°. Asymmetry angle and apical angle of trishear zone are 20° and 40°, respectively. X' is the trishear bisector, which corresponds to the 0° contour. Dash-dot lines represent the triangular boundaries of the backlimb trishear zone. The straight contour lines inside the trishear zone illustrate progressive velocity orientation changes.

between a flat and a 20° ramp. The trishear bisector can be located by the 0° contour. Because the velocity distribution across the trishear zone is linear, the contours are symmetric across the bisector. The contour plot also illustrates the 40° apical angle of the backlimb triangular wedge, which is bounded by the tangents to the outer-most contour lines (Fig. 4.1), as well as the asymmetry angle of 20° between the backlimb bisector and X'.

In the case of a fault-bend fold, the β contour displays three distinct features (Fig. 4.2). Straight contour lines diverge from the flat-ramp corners and connect above the ramp where the two trishear zones overlap. The interference results in curvilinear contour lines between the two trishear bisectors. When the two trishear zones are identical, the contour lines in the forelimb trishear zone are mirror images of those within the backlimb trishear zone.

Fig. 4.2 also shows that the interference between the two flat-ramp corners occurs within the overlap region. The location of the overlap region depends on ramp width, dip, and apical angle of the trishear zones. Below the overlap region, the 0° contour line matches well with the individual trishear bisectors.

4.2 β contour plot for the mechanical model

The β contour plots of the mechanical models are similar to those of the trishear model of the backlimb region of a fault-bend fold, at least to first approximation (Fig. 4.2). In all cases the β contours diverge from the flat-ramp corners and connect above the ramp. For an isotropic material or a horizontal anisotropy, the β contours are symmetric across the z axis. The contours from both corners connect at greater distance from the ramp as m increases. The symmetry of β contours across the z axis is destroyed with inclination of anisotropy. It can be seen that the β contours deviate most significantly from the trishear model with large m and large $|\alpha|$ (Fig. 4.3, 4.4, and 4.5). The greatest deviation is seen near the hinterland bend for inclination of anisotropy toward the foreland and near the foreland bend for inclination of anisotropy toward the hinterland.

4.3 Determination of trishear parameters for the mechanical models

The velocity distributions of the mechanical and trishear models, as shown by

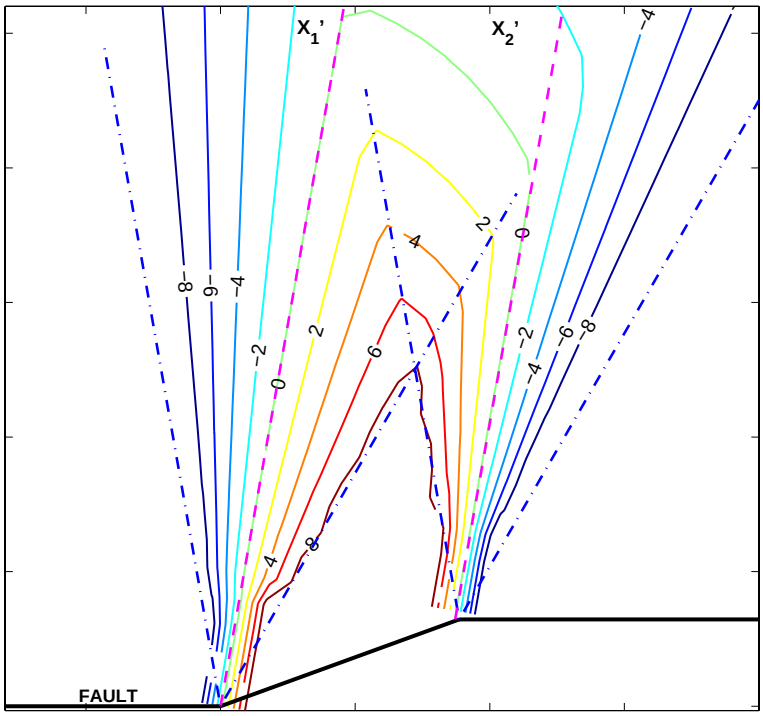

Fig. 4.2. Contour plot of the deviations of velocity from reference velocity for the trishear model of fault-bend fold . Two flat-ramp corners are separated by a fault ramp, whose dip angle is 20°. The asymmetry angle and apical angle of trishear zone are 20° and 40°, respectively. Dash lines X_1' and X_2' represent the trishear bisectors of backlimb trishear zone and a trishear zone at forelimb, respectively. The velocity along X_1' is set as reference velocity. Dash-dot lines represent the triangular boundaries of the two trishear zones.

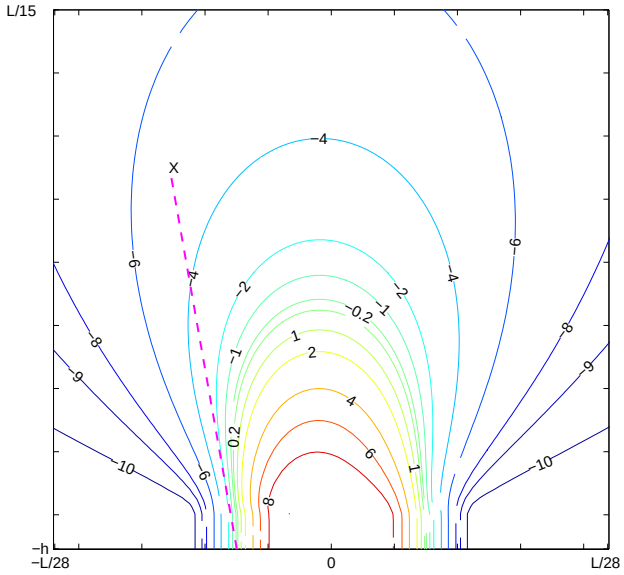

(a)

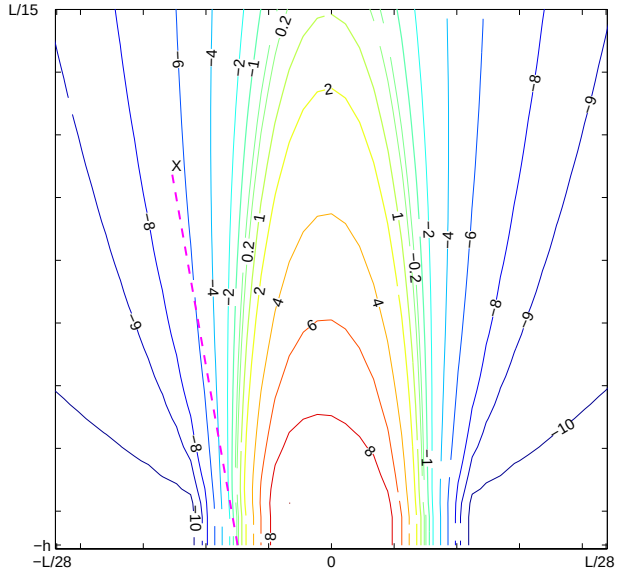

(b)

(c)

Fig. 4.3. Effect of magnitude of anisotropy on the distributions of β in the vicinity of an isolated thrust ramp. The maximum slope is 20° and $N = 100$. X represents the backlimb bisector. Contour intervals are -10,-9, -8, -6, -4, -2, -1, -0.2, 0, 0.2, 1, 2, 4, 6, 8, 9 and 10. (a) Contour plot of β for the case of isotropic media ($m = 1, \alpha = 0°$). (b) Contour plot of β for the case of anisotropic media ($m = 10, \alpha = 0°$). (c) Geometry of the sliding surface.

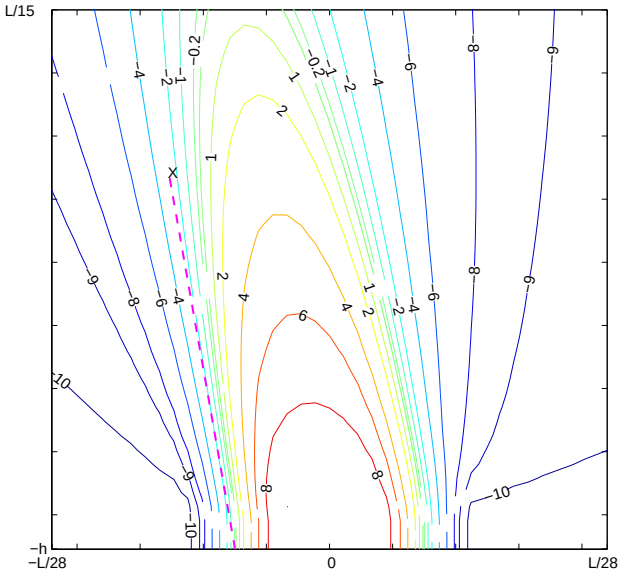

(a)

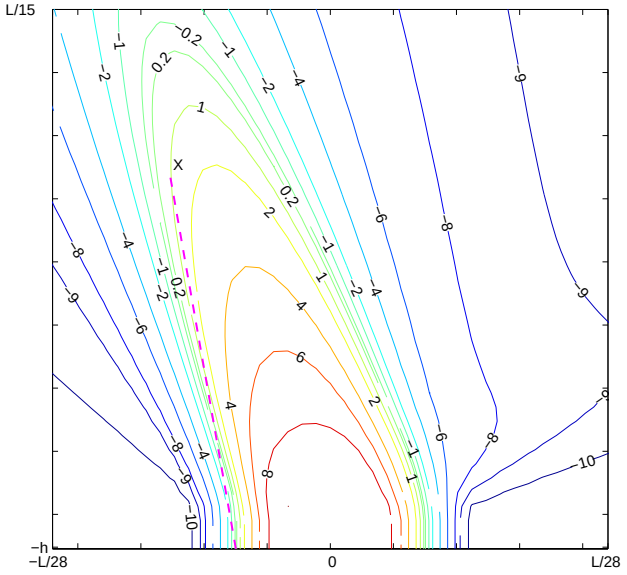

(b)

(c)

Fig. 4.4. Effect of orientation of anisotropy on the distributions of β in the vicinity of an isolated thrust ramp. X' represents the backlimb bisector. The maximum slope is 20° and $N = 100$. Contour intervals are -10, -9, -8, -6, -4, -2, -1, -0.2, 0, 0.2, 1, 2, 4, 6, 8, 9 and 10. (a) Contour plot of β for the case of $m = 10$ and $\alpha = 10°$. X represents the backlimb bisector. (b) Contour plot of β for the case of $m = 10$ and $\alpha = 20°$. (c) Geometry of the sliding surface.

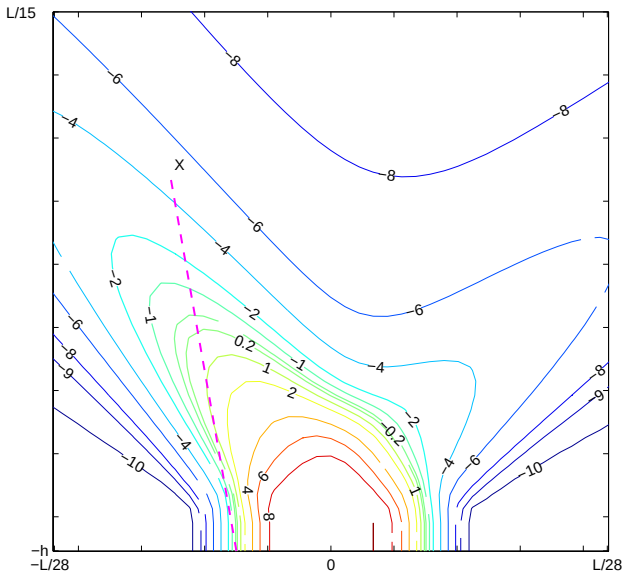

(a)

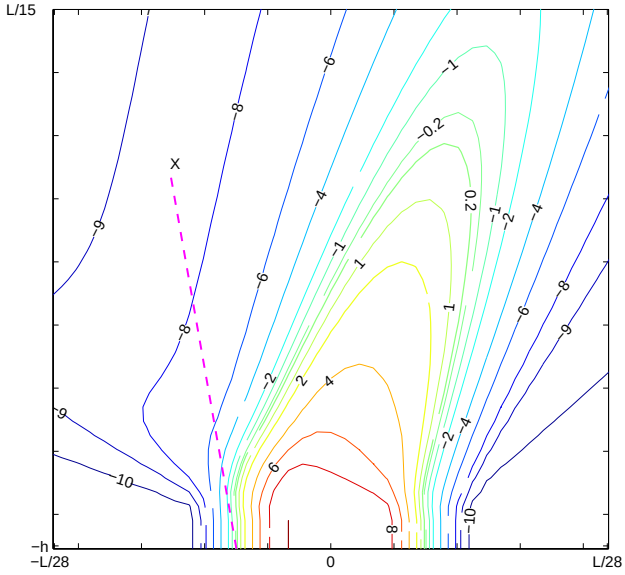

(b)

(c)

Fig. 4.5. Effect of orientation of anisotropy on the distributions of β in the vicinity of an isolated thrust ramp. X represents the backlimb bisector. The maximum slope is 20° and $N = 100$. Contour intervals are -10, -9, -8, -6, -4, -2, -1, -0.2, 0, 0.2, 1, 2, 4, 6, 8, 9 and 10. (a) Contour plot of β for the case of $m = 10$ and $\alpha = 40°$. (b) Contour plot of β for the case of $m = 10$ and $\alpha = -20°$. (c) Geometry of the sliding surface.

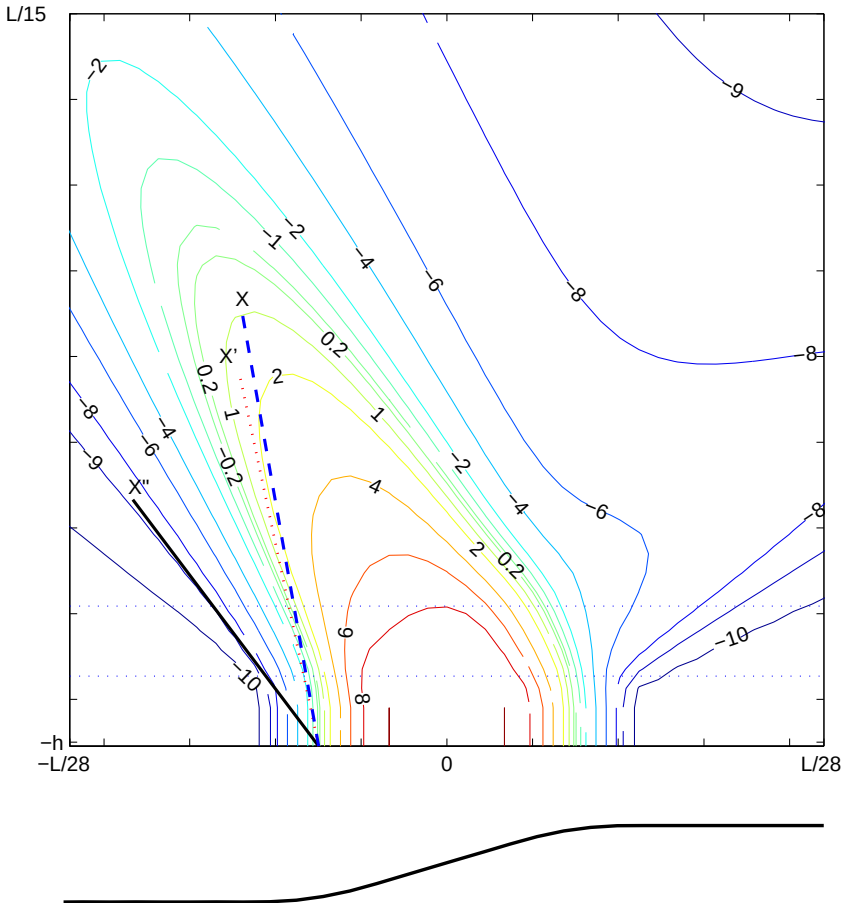

Fig. 4.6. The deviations of backlimb velocity from reference velocity (β) for the case of anisotropic media ($m = 10, \alpha = 30°$) in the vicinity of an isolated thrust ramp. The maximum slope is 20° and $N = 100$. Geometry of the sliding surface is shown at the bottom of figure. See text for discussions of X, X', and X''. Two horizontal dot lines represent the $z = 3H/2$ and $z = 3H/4$, respectively. The contour lines inside the trishear zone illustrate progressive but non-linear variations in velocity orientations. Contour intervals are -10, -9, -8, -6, -4, -2, -1, -0.2, 0, 0.2, 1, 2, 4, 6, 8, 9 and 10.

the β contour plots, are similar. Accordingly, it is possible to approximate the velocity distribution of the mechanical model using trishear kinematics, and to pick the appropriate trishear parameters from the β contour plots. Due to the interference between the upper and lower ramp corners, only the velocities in the hinterland flat-ramp bend are used to determine the trishear parameters. By locating the trishear bisector X' and the hinterland boundary of the trishear zone, one can infer α_{ca} and φ. In this procedure we assume the trishear zone is symmetric about X' and thus can use 2φ as the trishear apical angle.

To standardize the picking of trishear parameters, we assume the trishear bisector and trishear boundary must pass through the flat-ramp corner and coincide with the 0° and -9°, respectively (Fig. 4.6). Because the contour lines are curved, we pick the locations of the contour lines at $z = 3H/4$ and $z = 3H/2$ to define the exact location of the trishear bisector and boundary.

Table 4.1. Matrix of β contours for the mechanical model when $N = 100$.

m	Ramp slope	α	2φ	α_{ca}	Figure Number
1	20°	0°	76°	7.5°	4.3a
10	20°	0°	56°	10°	4.3b
10	20°	10°	49°	5°	4.4a
10	20°	20°	52°	1°	4.4b
10	20°	30°	50°	-2°	4.6
10	20°	40°	58°	-2°	4.5a
10	20°	-20°	96°	18°	4.5b

4.4 Relations between trishear and mechanical parameters

Trishear parameters were determined from β contour plots of the mechanical

model using 20° ramp dip and angularity $N = 100$, and numerous combinations of m and α in the range of $1 \leq m \leq 100$ and $-45° \leq \alpha \leq 45°$. Examples of trishear parameters determined from β contour plots of the mechanical model shown in Fig. 4.3, 4.4, 4.5, and 4.6 are listed in Table 4.1.

The relationships between mechanical parameters and trishear parameters are illustrated graphically in Fig. 4.7 to 4.12. In general the relationships for trishear parameters picked at $z = 3H/4$ are poorly behaved and not systematic. This may reflect that the depth of $z = 3H/4$ is too close to the mean plane of the sliding surface.

In contrast, trishear parameters picked at $z = 3H/2$ are very systematic with respect to the mechanical parameters. The trishear asymmetry angle strongly depends on orientation of the anisotropy, but also is affected by magnitude of anisotropy. In general asymmetry is most positive for moderate inclination to the foreland and most negative for moderate inclination to the hinterland. The mechanical models predominantly predict positive asymmetry. The greatest magnitude of asymmetry is seen in models with the greatest magnitude of anisotropy.

Trishear apical angle also varies with inclination of anisotropy, but shows a strong dependence on the magnitude of anisotropy. In general, apical angle decreases with increase in anisotropy. The smallest apical angle are produced by mechanical models with large anisotropy and inclination of anisotropy toward the hinterland. The largest apical angle occur for large anisotropy magnitude inclined toward the foreland. Apical angle for the isotropic case is generally between $75 - 80°$.

Fig. 4.11 provides the best summary of the relationship between the mechanical parameters and the backlimb trishear parameters. The variations of α_{ca} are represented by the solid contour lines, and the variations of 2φ are represented by the dash-dot lines. The contour lines of α_{ca} in most of the figure are sub-vertical, suggesting that the dominant parameter that affects α_{ca} is α. Contours of 2φ show that apical angle primarily depends on the magnitude of anisotropy.

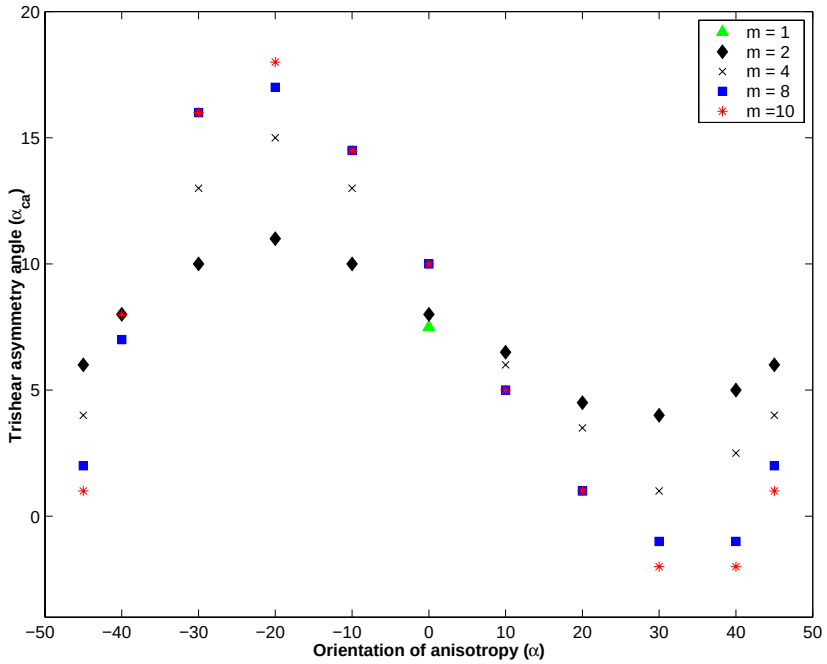

Fig. 4.7. Scatter plot of the relationship between the orientation of anisotropy (α) and the backlimb asymmetry angle (α_{ca}). Data collected at $z = 3H/2$. The maximum slope of ramp is 20° and $N = 100$.

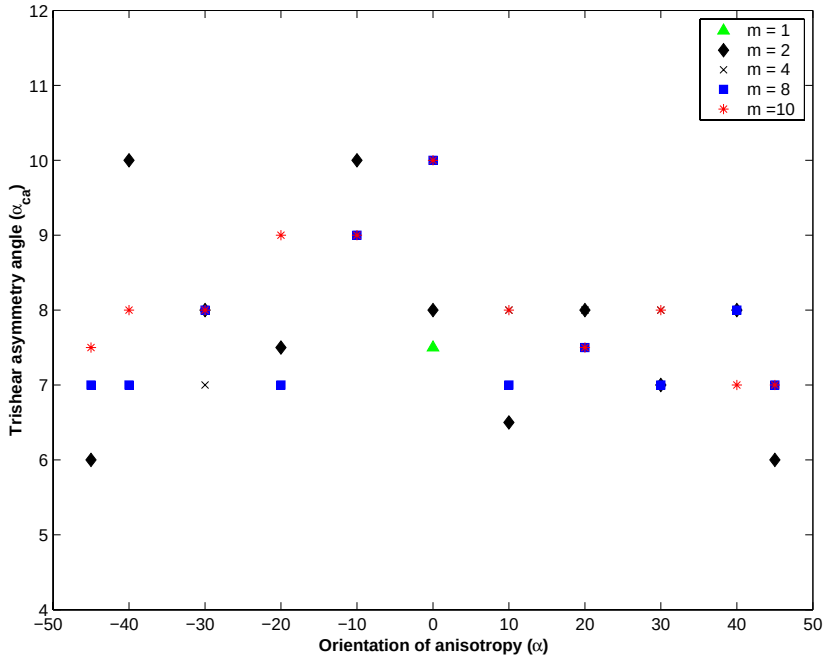

Fig. 4.8. Scatter plot of the relationship between orientation of anisotropy (α) and the backlimb asymmetry angle (α_{ca}). Data collected at $z = 3H/4$. The maximum slope of ramp is 20° and $N = 100$.

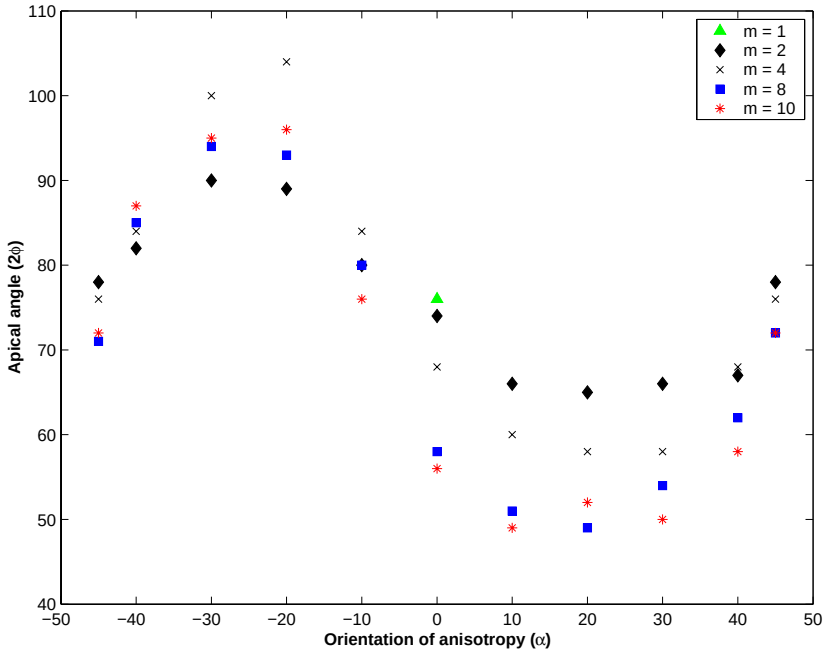

Fig. 4.9. Scatter plot of the relationship between α and apical angle of triangular zone in the vicinity of an isolated thrust ramp. Data collected at $z = 3H/2$. The maximum slope of ramp is 20° and $N = 100$.

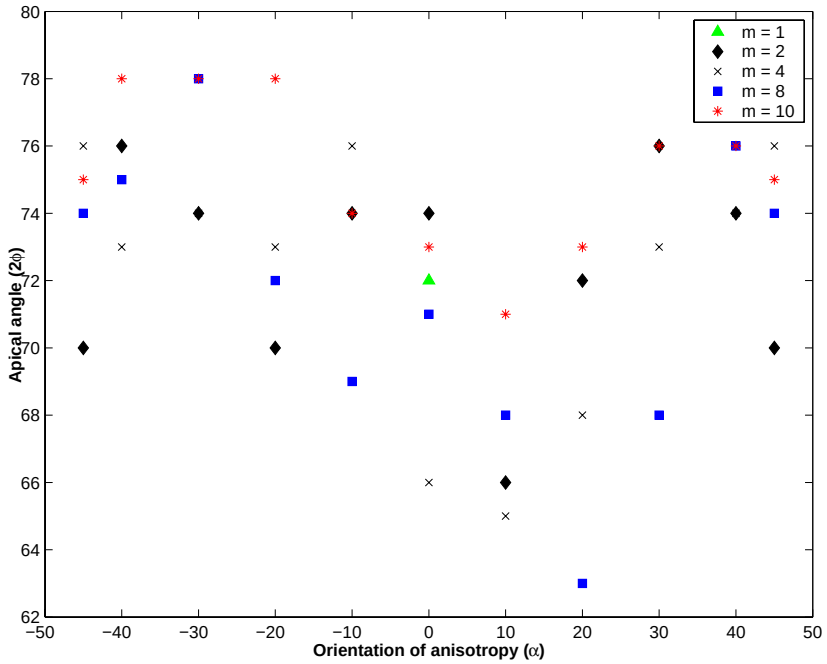

Fig. 4.10. Scatter plot of the relationship between α and apical angle of triangular zone in the vicinity of an isolated thrust ramp. Data collected at $z = 3H/4$. The maximum slope of ramp is 20° and $N = 100$.

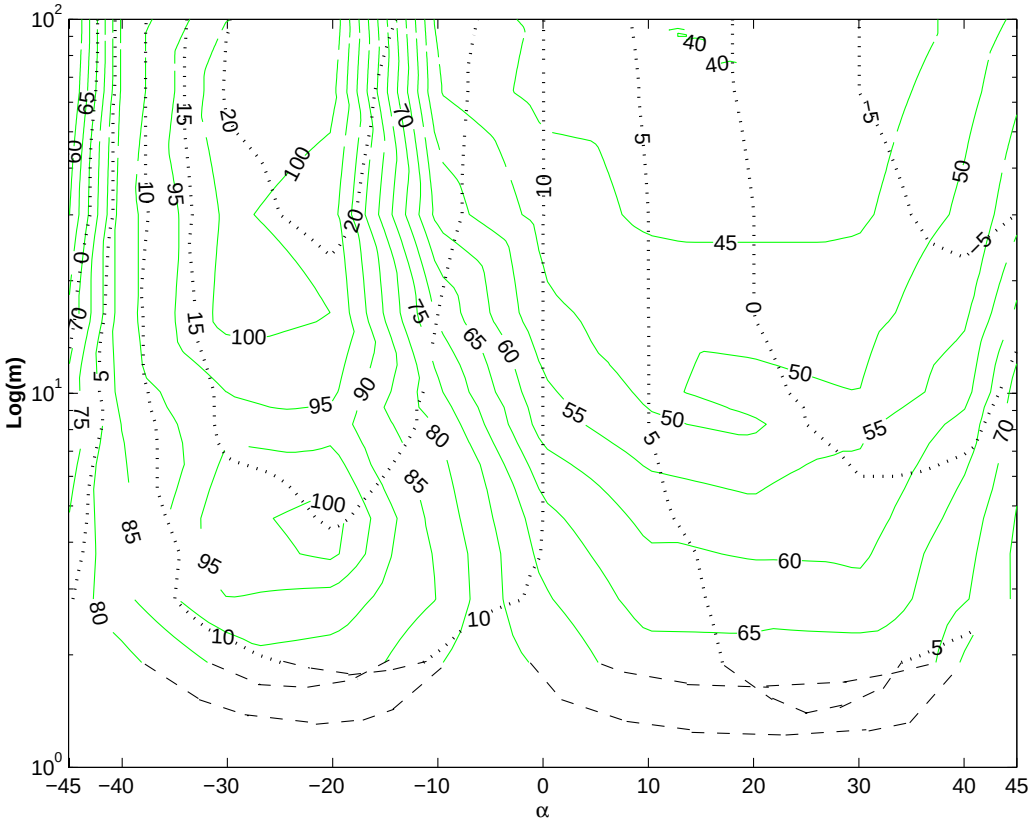

Fig. 4.11. The correlations between mechanical parameters and backlimb trishear parameters when the maximum slope of angular fault is 20°. All data are collected at $z = 3H/2$. The contour lines relate magnitude of anisotropy (m) to the orientation of anisotropy (α). m is mapped in a logarithmic scale from 1 to 100. Dot lines are the contour lines of backlimb asymmetry angle (α_{ca}). Solid lines represent the variations of trishear apical angle. The dash lines are interpretations.

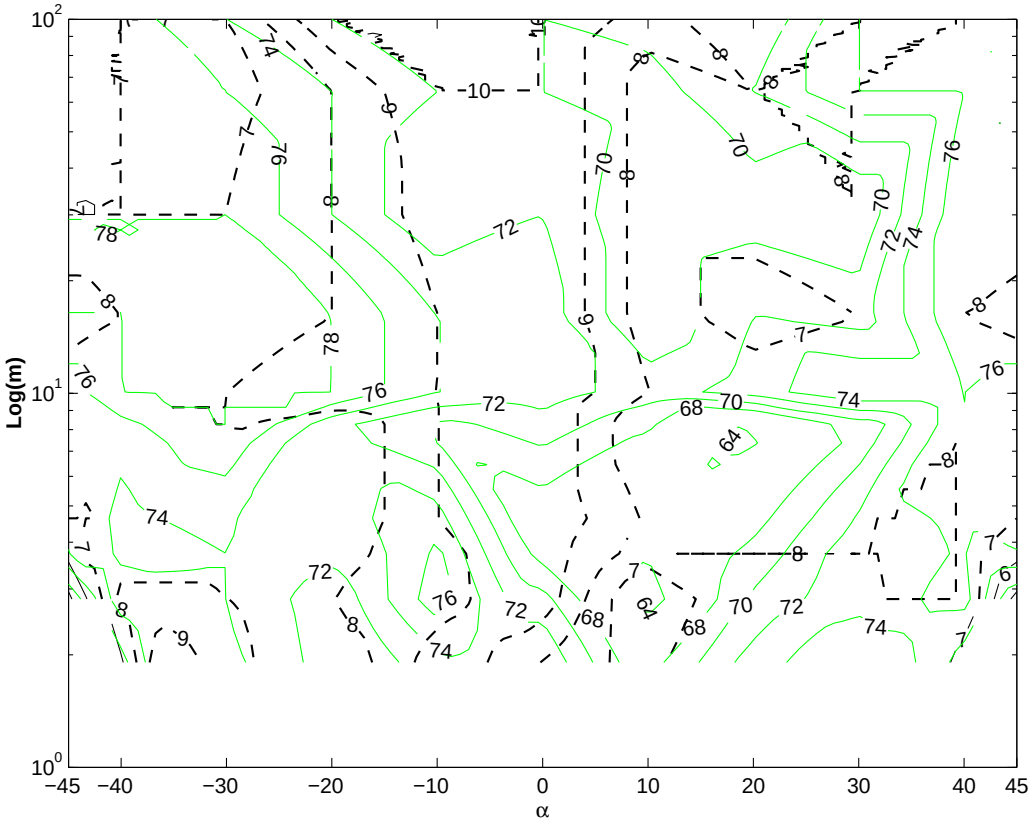

Fig. 4.12. The correlations between mechanical parameters and backlimb trishear parameters when the maximum slope of angular fault is 20°. All data are collected at $z = 3H/4$. The contour lines relate magnitude of anisotropy (m) to the orientation of anisotropy (α). m is mapped in a logarithmic scale from 1 to 100. Dash lines are the contour lines of backlimb asymmetry angle (α_{ca}). Solid lines represent the variations of trishear apical angle.

CHAPTER V

APPLICATION TO PHYSICAL MODELS AND NATURAL EXAMPLES OF FAULT-BEND FOLDS

5.1 Philosophy of the approach

Normally, we do not have a direct link between mechanical parameters and the geometries of physical or natural examples of fault-bend folds. However, kinematic models (e.g., backlimb trishear) establish a simple link between kinematic parameters and the geometry of natural structures. We have established a correlation between mechanical parameters and kinematic parameters (Fig. 4.11). Using this relation, we infer the mechanical properties of two analog models of natural fault-bend folds and one natural example. To make the comparison, we first approximate the geometry of each fault-bend fold with the trishear model to determine the apical and asymmetry angles of the trishear zone. Then using our relation presented in Fig. 4.11, we determine the magnitude of anisotropy of the model and natural sequences. Of course, this method is only as sound as the appropriateness of the kinematic and mechanical models to the natural deformations (e.g., Cristallini and Allmendinger, 2002).

5.2 Analysis of analog models

To test the approach of infering mechanical properties for fault-fold structures using the relationship between kinematic and mechanical parameters, we analyze analog models of fault-bend folds for which the magnitude of anisotropy can be estimated independently using published rock mechanics data for the same model materials (Chester et al., 1991).

Physical models of fault-bend folds have been used to investigate the effects of boundary conditions and heterogeneous layering on the development of fold geometry and mechanics (e.g., Morse, 1977; Chester et al., 1991). These models produce rounded fold geometries in the hanging-wall above angular fault bends.

Morse (1977) investigated hanging-wall deformation above a ramp segment of a thrust fault for an isotropic hanging-wall case. The model configurations consist of

a rigid granite block, a thick layer of Coconino sandstone with a 20° precut ramp, and a solid layer of overlying Indiana limestone (Fig. 5.2). The style of hanging-wall deformation in the model fault-bend folds agrees well with Rich (1934)'s hypothesis and Serra's (1977) mode III configuration. In the isotropic case the hanging-wall thickened by backthrusting as it moved through the lower ramp hinge.

Chester et al. (1991) and Chester (1985) use two configurations similar to Morse (1977), but in which the hanging-wall is distinctly anisotropic. These latter models consist of a rigid block of Tennessee Sandstone, a precut 20° Coconino sandstone ramp, and a thinly layered veneer of interlayered Indiana limestone, lead and Coconino sandstone (Fig. 5.3). When thin layers are incorporated throughout the hanging-wall, backthrusting at the lower ramp hinge is less pronounced and the fold form is more rounded (Chester 1985). Morse (1977) and Chester et al. (1991) demonstrate that these fractures form at the lower hinge and move up the backlimb.

The mechanical properties of the analog model are not simple. However, we may characterize the degree of anisotropy for the layered hanging-wall package following the methodology of Biot (1965), Johnson and Fletcher (1994), Patton and Fletcher (1998a, b), and Chester and Fletcher (1997) for multilayers. If we assume a viscous rheology, the anisotropy of the multilayered package that consists of alternating stiff and soft layers (Fig. 5.1) can be characterized by the effective shear viscosity, μ_s, and effective normal viscosity, μ_n, as given by

$$\mu_n = [1/(t_1 + t_2)](t_1\mu_1 + t_2\mu_2) \tag{5.1}$$

$$\mu_s = (t_1 + t_2)\mu_1\mu_2/(t_1\mu_2 + t_2\mu_1) \tag{5.2}$$

where μ_1, t_1 and μ_2, t_2 are viscosities and thickness of the stiff and soft materials, respectively. The magnitude of anisotropy or viscosity contrast, m, is defined as the ratio of μ_n/μ_s (Johnson, 1977).

We will assume that μ_s ad μ_n can be defined by the ultimate or yield strength (defined at 4% strain) of the material when deformed under similar pressure and temperature conditions. Using published data (Chester et al., 1991), the strength of the sandstone, limestone, and lead layers are estimated as 210 MPa, 100 MPa, and 12 MPa, respectively.

Alternatively, we can idealize the anisotropic behavior of the packages in the analog models by assuming a plastic rheology. When subjected to layer-parallel shearing,

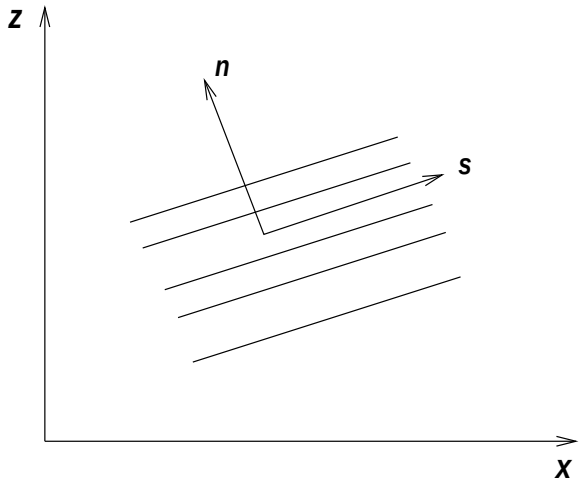

μ2	t2
μ1	t1
μ2	t2

Fig. 5.1. Element of planar anisotropy. Multilayer consists of stiff (1) and soft (2) materials. The planar anisotropy is assumed to be inclined with respect to x axes. Local coordinates n and s are perpendicular and parallel to the plane of anisotropy, respectively. Diagram adapted from Johnson and Fletcher (1994).

the shear strength in stiff and soft layers are different. Shear of the multilayer is dictated by the soft layer, and will be favored for loads directed at 45° to the multilayer. Whereas, the strength of the package will be governed by the strong layers when loaded parallel or perpendicular to the layering. In this idealization, the effective normal strength, σ_n, and effective shear strength, σ_s, are defined as:

$$\sigma_n = [1/(t_1 + t_2)](t_1\sigma_1 + t_2\sigma_2) \tag{5.3}$$

$$\sigma_s = \sigma_2/2. \tag{5.4}$$

where σ_1, t_1 and σ_2, t_2 are the strength and thickness of stiff and soft materials, respectively. The magnitude of anisotropy or strength contrast is defined by the ratio of σ_n/σ_s.

5.2.1 Application to Morse (1978) #II-403

The stiff material in Morse's (1978) experiment (#II-403) is Coconino sandstone, and the soft material is Indiana limestone. Using the expressions for viscous materials and the thicknesses of each material, we calculate the magnitude of anisotropy for Morse's (1977) experiment to be 1.14, which approaches an isotropic value. The degree of anisotropy using a plastic rheology is calculated to be 3.12.

Cristallini and Allmendinger (2002) simulate Morse's (1978) analog model (Fig. 5.2) with a backlimb trishear zone apical angle of 50° and asymmetry of −25°. Considering that the fractures are generated inside backlimb trishear zone and then migrate up the ramp, the backlimb trishear kinematics compare well with the analog model.

The 50° contour line in Fig. 4.11 indicates that the range of α is likely from −10° to 40°. However, we fail to infer the magnitude of the anisotropy because $\alpha_{ca} = -25°$ contour is not presented in the correlation (Fig. 4.11).

The range of acceptable asymmetry angle for the trishear model of a fault-bend fold with ramp dip of 20° is about −60° to 60°. Whereas, the range predicted by the mechanical model with ramp dip of 20° is about −8° to 23° (Fig. 4.11). The mechanical model assumes an incompressible viscous media, whereas the rheology of the rock model of Morse (1978) is not viscous. The rock model consists of thick bulk Indiana limestone and Coconino sandstone layer, instead of thin alternating stiff and soft materials as the Chester and Fletcher (1997) mechanical model assumes. The Morse (1978) rock model displays significantly more negative asymmetry than these

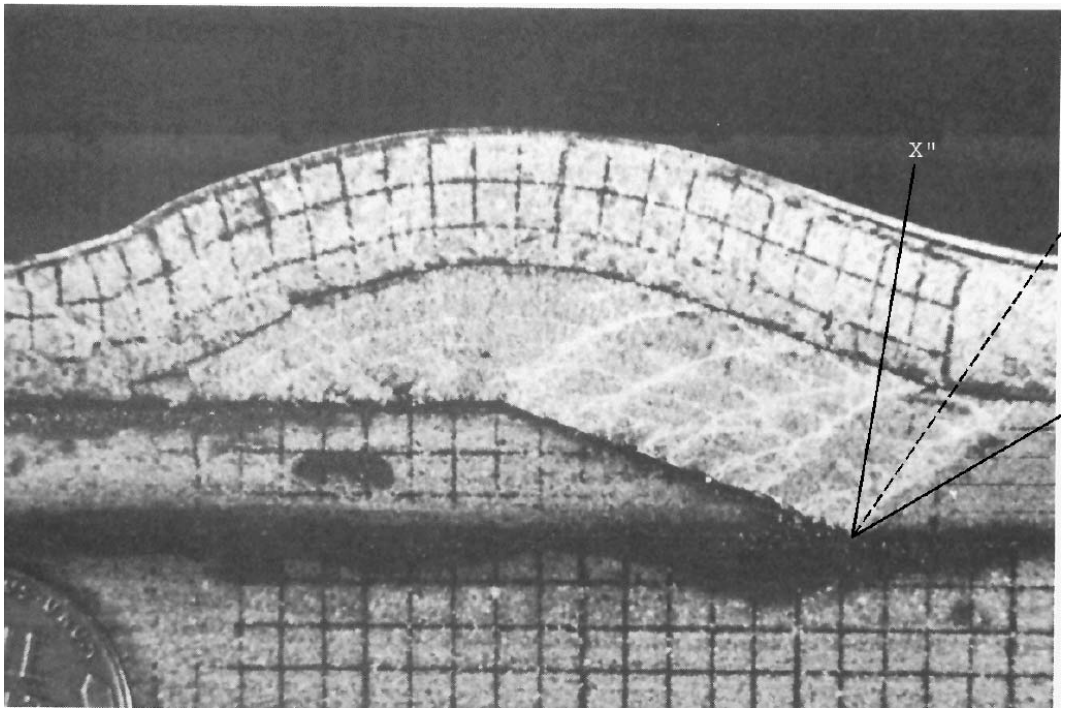

Fig. 5.2. Deformation map of Morse (1977) configuration H experiment (Specimen II-403). Ramp height is 0.8 cm. Thicknesses of Indiana limestone and Coconino sandstone are 0.73 and 0.76cm, respectively. Solid lines represent the superposed trishear boundaries. Dash line represents the trishear bisector. The apical angle and asymmetry angle of trishear zone are 50° and −25°, respectively.

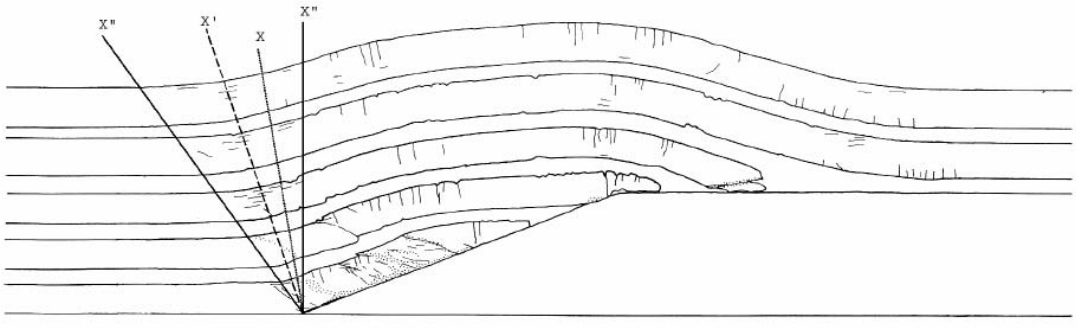

Fig. 5.3. Deformation maps of configuration specimen #1809. Interlayered lead, limestone and sandstone veneer with shortening/ramp width ratio (S/L_r) of 0.56. The thickness of each Coconino sandstone layer is 0.063 inch. The thickness of each Indiana limestone is 0.076 inch, and the average thickness of lead layers is 0.03 inch. X, X', and X'' represent the backlimb bisector, the trishear bisector, and the superposed trishear boundaries, respectively. The apical angle and asymmetry angle of trishear zone are 36° and −8°, respectively.

predicted by the mechanical model for the same magnitude of anisotropy.

5.2.2 Application to specimen #1809 of Chester (1985)

The deformation map of specimen #1809 (Chester, 1985) is shown in Fig. 5.3. Specimen #1809 consists of three layers of pre-cut Coconino sandstone, separated by two thin layers of lead, and a overlaying relatively weak limestone/lead multilayer veneer. The multilayered veneer consists of two layers of Indiana limestone and two thinner layers of lead.

The equations of anisotropic behavior only consider two relatively stiff and soft materials interlayered with each other. However, specimen #1809 includes three materials in its hanging-wall. Assuming a viscous rheology, we consider two end-members to approximate the anisotropy of a package containing three materials using Johnson and Fletcher (1994) equations. First, the veneer consists of limestone and lead layers, whose thicknesses are 0.076 inch and 0.03 inch, respectively. This case yields an estimation of strength contrast of 2.31. The second case considers lead whose average thickness is 0.03 inch and Coconino sandstone layers of 0.063 inch interlay with each other. The strength contrast of the second case is 4.4. The magnitude of anisotropy of this analog model is estimated to be between 2.31 to 4.4.

Assuming a plastic rheology, the two end-member values of anisotropy magnitude are estimated to be 12.54 and 24.35.

In an effort to fit specimen #1809 with a backlimb trishear model, both layer thickness changes and layer orientation are taken into consideration. The trishear bisector X' is defined as the hinge of a kink-band fold. The hinterland trishear boundary connects the deviation point in the backlimb and the lower fault bend. The orientation of the hinterland trishear boundary is subparallel to the backthrusts in the backlimb of the specimen. An apical angle of 36° and asymmetry of -8° (Fig. 5.3) fit well with the specimen.

The correlation between the mechanical parameters and backlimb trishear parameters (Fig. 4.11), indicates that when backlimb trishear zone parameters are $2\varphi = 36^\circ$ and $\alpha_{ca} = -8^\circ$, the magnitude of anisotropy of anisotropic fault-fold system is about 100 and the orientation of anisotropy is 45°.

The Chester's (1985) specimen consists of thin alternating stiff and soft layers of material, the anisotropy of this rock model approximates that of the mechanical

model. The asymmetry angle of this specimen is within the range that the mechanical model predicts.

The calculation based on a plastic rheology yields higher magnitude of anisotropy than calculation based on a viscous rheology. The magnitude of anisotropy based on the plastic rheology is closer to what predicted in Fig. 4.11.

5.3 Applications to Lost Hills anticline at SE Lost Hills, San Joaquin Basin, CA

5.3.1 Previous structural analysis of Lost Hills anticline

Previous structural analysis of folds along the western side of the San Joaquin Valley suggests that folds are formed by the process of fault-bend folding or fault-propagation folding (Namson and Davis, 1988; Medwedeff, 1989).

Lost Hills anticline (Fig. 5.4) is located in the southern end of the fold-thrust belt bounded by the San Andreas fault and San Joaquin basin. The strike of Lost Hills anticline is approximately parallel to the San Andreas fault. Based on the construction of retrodeformable cross-sections, well and seismic data, Medwedeff (1989) analyzed the Lost Hills anticline and suggested that it is a growth fault-bend fold that steps up from the base of the Tertiary to the Reef Ridge Formation.

Medwedeff (1989) assumed a perfectly angular fold geometry and located the axial surfaces of the fault-bend fold by assuming constant bed thickness in pre-growth strata and flat horizons in the adjacent basin. His structural analysis presents the geometric features of the Lost Hills anticline as an upright, asymmetric anticline. The forelimb dips about 42° and backlimb dips about 27°. The crest of the anticline is nearly horizontal, which is approximately 3 km wide. The size of the structure is 32 km long and 10 km wide, and its structural relief is 2.1 km above the San Joaquin basin. The upper and lower detachments locate at 4 km and 6 km depths, respectively. Medwedeff's (1989) interpretation suggests that displacement on the lower detachment is about 6.5 km.

In a later review by Medwedeff (2000), he indicates that the observed growth pattern at the Lost Hills anticline can probably be explained with the trishear model of Hardy and Ford (1997).

The idea that Lost Hills anticline may be a natural example of a growth backlimb

trishear model is inspired by Medwedeff (2000) and the two features presented by Medwedeff (1989). First, the basinal sediment rotation only happens at the backlimb region of Lost Hills anticline. This is consistent with the backlimb trishear model assumption that the area of bed rotation is constrained within a triangular zone at the backlimb. Second and more importantly, the fold form is rounded and has sharper curvature near the fault. These observations match backlimb trishear model simulations. The sharper curvature near the fault could be a result of constrained bed rotation within the backlimb trishear zone (Cristallini and Allmendinger, 2002).

5.3.2 Degree of anisotropy presented in the pre-growth portion of Lost Hills anticline

Inverting of backlimb trishear parameters of the Lost Hills anticline can be done by finding the trishear bisector and the triangular zone boundaries. The trishear bisector X' is found by locating the hinge of the pre-growth strata of the anticline (Fig. 5.5a). The migrated seismic section indicates that the backlimb dip of the Reef Ridge strata is about 23°. By assuming constant bed thickness in pre-growth strata and flat horizons in the adjacent basin, the fault angle is approximately 23°. The seismic section was limited in the SW direction, and large thickness change are apparent. It is not clear the cause of the thickening. We then identify the trishear boundary and trishear parameters of the backlimb by the forelimb trishear parameters. The triangular boundaries (X'') of the forelimb trishear zone are picked at points where the strata deviate from horizontal in the backlimb and the crest. Following the definitions above, the geometry of pre-growth portion of Lost Hills anticline is fit with apical angle of 58° and asymmetry of $-2°$.

Medwedeff (1989) indicated that the layers have a uniform dip and thickness on the backlimb. These features imply a symmetric or a slightly asymmetric backlimb trishear zone, in which only slight changes occur in layer thickness. The asymmetry angle for the Lost Hills anticline defined above is a small angle, in agreement with the geological observations.

The correlation in Chapter IV (Fig. 4.11) is suitable for a fault-bend fold with a 20° ramp. Although the fault angle in the Lost Hills anticline is 23°, Fig. 4.11 still works to some extent. It suggests that the magnitude of anisotropy presented in this structure is about 26, and the orientation of anisotropy is about 42°.

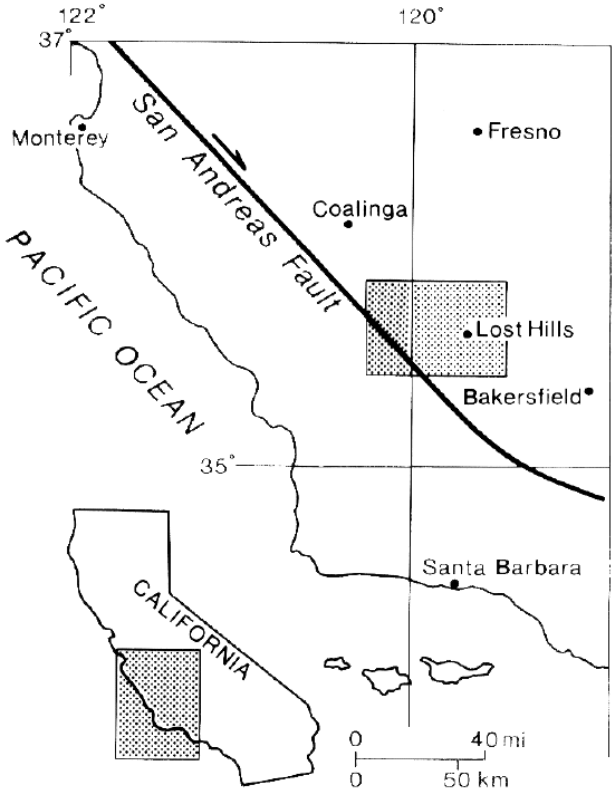

(a)

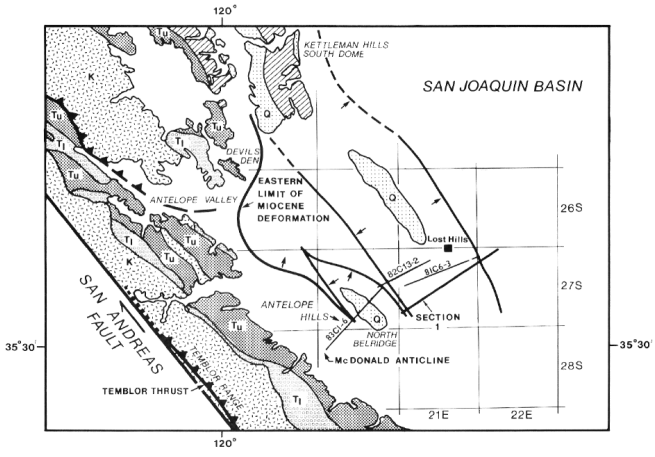

(b)

Fig. 5.4. Geology map of Lost Hills anticline, CA. (a) Location map study area.(b)Close-up view of Lost Hills. Seismic sections 81C6-3, 81C1-6, and 82C13-2 are indicated in figure. Map after Medwedeff (1989).

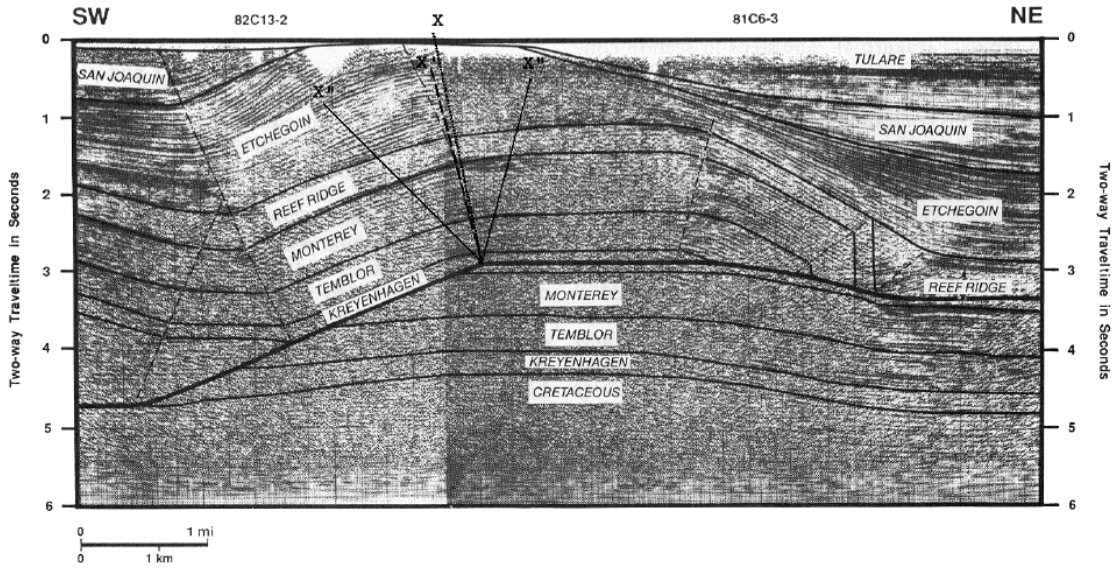

(a)

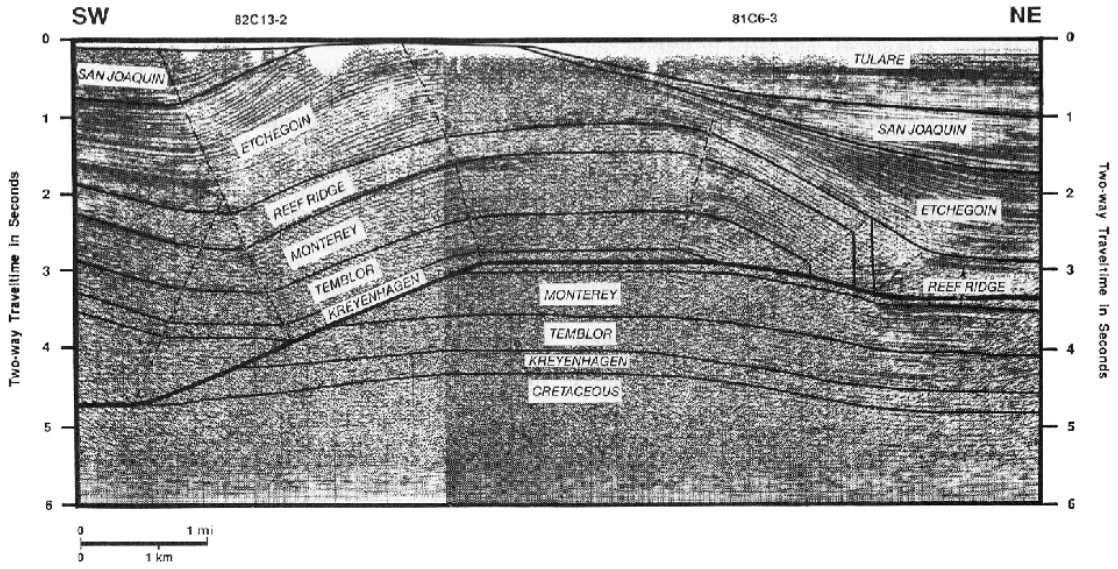

(b)

Fig. 5.5. Seismic sections of Lost Hills anticline. Migrated time section. Vertical and horizontal scales are approximately equal. (a) Interpretation with the backlimb trishear kinematics. X, X', and X'' represent the backlimb bisector, the trishear bisector, and triangular boundary, respectively. (b) Medwedeff's (1989) interpretation. Unconformity begins within Etchegoin Formation and ends at the top of San Joaquin Formation. Seismic lines from Medwedeff (1989).

Sherwin and Chapple (1968) found that the viscosity ratios for 818 small single layer folds from 6 locations range from 14 to 30. The magnitude of anisotropy (viscosity contrast) of the Lost Hills anticline predicted in our analysis is within that range.

CHAPTER VI

CONCLUSIONS

6.1 Comparison and correlation between two models

In many ways, the backlimb trishear model resembles the mechanical model of Chester and Fletcher (1997). As described in Chapter III, the velocity distributions in the backlimb regions and the rounded backlimb geometry are common features. Bed thickness changes are observed in both models. The thickening or thinning of beds occurs within a deformation-concentrated zone bounded by two triangular boundaries and the deformed layers move up the ramp as displacement accumulates.

As constructed, the backlimb trishear kinematic model does not have a mechanical basis. Cristallini and Allmendinger (2002) have shown that an infinite number of velocity fields satisfy the backlimb trishear boundary conditions and area conservation assumption. The comparison and correlation between the Chester and Fletcher (1997) mechanical model and the backlimb trishear model help us determine the conditions under which the trishear model is an acceptable approximation of the deformation and select the trishear parameters for subsurface structural interpretations in fault-fold terrains.

In the backlimb trishear model, a triangular zone of distributed shear exists at the lower fault bend of a fault-bend fold. The reason for the triangular shear zone, as Allmendinger (1998) indicates, must lie in the mechanics of trishear. However, the physical conditions that determine whether a trishear zone occurs were not well understood. Both the backlimb trishear asymmetry angle and apical angle are free variables. The physical property that may control these parameters is still not clear (Allmendinger, 1998).

The analysis in Chapter IV indicates a strong correlation between the orientation of anisotropy and the asymmetry angle of the trishear zone. The distributed deformation pattern presented at the backlimb region of a fault-bend fold likely results from the properties of the sedimentary sequences. This relationship depends on both the magnitude and orientation of anisotropy. However, the orientation of material anisotropy plays a more important role than the magnitude. The variations of the

trishear asymmetry angle are sub-vertical, suggesting subordinate effects result from the magnitude of anisotropy (Fig. 4.11).

There is a strong correlation between the magnitude of anisotropy and the trishear apical angle for each data set in Fig. 4.9. In general, increasing value of m is associated with a decrease in the opening of triangular region. Fig. 4.9 also shows that the magnitude and orientation of material anisotropy are mechanical properties that affect the trishear apical angle.

The velocity solution for the mechanical model is derived for an incompressible viscous rheology, based on the equations of equilibrium and strain rate compatibility equation. This ensures the mechanical model is physically tenable. However, the validity of the assumptions of the mechanical model must be evaluated. The nature of the first-order approximation in the mechanical models requires that the maximum slope of the ramp be smaller than 20°. Whereas in the backlimb trishear model, there is no rheology condition of the deforming media or geometric limit besides the area conservation assumption. The comparison and correlation between these two models indicate that the mechanical model is analogous to the backlimb trishear model under certain conditions. When the deforming media is incompressible and viscous, the backlimb trishear model with ramp angle less than 20° is an acceptable approximation to the mechanical model.

For inclined anisotropic material, the concentration bands in the β contour plot for the mechanical model are asymmetric except in the limit case of 45°. In this case, the concentration bands are symmetric and result in increasingly similar contour lines in Fig. 4.11 as $|\alpha|$ approaches 45°. This has posed a question for further research. For the mechanical model, what is the relationship between the backlimb trishear zone and the forelimb trishear zone? Are they identical? As all data are collected at the lower hinge, it is worth exploring the correlation for data at the upper hinge using the foreland trishear boundary.

6.2 Application to the physical models and natural structure

The result of this study can be applied to physical models of fault-bend folding to infer the magnitude and orientation of anisotropy of the material components of the physical model. The applicability of current results obtained from the correlation plot can be checked by comparing them with results predicted with the equations of plane

anisotropy (Johnson and Fletcher, 1994). Differences are expected, mainly because the calculations approximate the anisotropy of the lithic package containing three materials with contrasting rheology using equations concerning only two interlayering stiff and soft materials. Another uncertainty comes from the method for inverting data on physical models for a best-fit backlimb trishear model without a statistical basis (e.g. least squares regression as in Allmendinger, 1998). However, the comparison provides insights on the sensitivity of current results.

Under the experimental conditions of Morse (1978) or Chester (1992), the lead simulates a relatively weak and ductile lithologic unit such as salt or shale. The Indiana limestone is relatively competent, isotropic brittle layer.

The Morse (1977) specimen contains a thick layer of pre-cut Coconino sandstone and a solid layer of Indiana limestone. The fold-thrust structure produced is the Rich geometry with rounded hinges. The limestone layer conforms to the sandstone unit, inside of which contains backthrusts and microfractures. When limestone is interlayered with Coconino sandstone, the package is nearly isotropic. Utilizing the correlation between mechanical parameters and trishear parameters, we predict that the orientation of anisotropy ranges from -10° to 40°.

Specimen #1809 consists of multiple thinner layers of Coconino pre-cut layers and an overlaying relatively weak limestone/lead veneer. This configuration eliminates the effect of a bulk strong Coconino sandstone unit. The layering geometry is closer to the ideal interlayering geometry as described in Fig. 5.1. The calculation of strength contrast based on a plastic rheology yields value that is closer to what predicts from Fig. 4.11 than that of a viscous rheology.

Our prediction to magnitude and orientation of anisotropy in the Lost Hills anticline suggests that the sedimentary sequences are highly anisotropic. The magnitude and orientation of the planar anisotropy in this structure is likely 26 and 42°, respectively. The predicted magnitude of anisotropy of this structure is within the range of viscosity constrast Sherwin and Chapple (1968) found.

6.3 Conclusions

As a result of the study of providing a mechanical basis to the backlimb trishear kinematic models using the Chester and Fletcher (1997) mechanical model, and correlating the mechanical properties and kinematic properties and of predicting

the magnitude of anisotropy utilizing the correlation, the following conclusions are reached.

1. When the deforming media is incompressible and viscous, the backlimb trishear model with ramp angle less than 20° is analogous to the mechanical model.

2. The apical angle, asymmetry angle and overall geometry of the hanging-wall syncline above the ramp depend on the magnitude and orientation of the planar anisotropy inherent in stratigraphic sequences.

3. The asymmetry of trishear zone in the backlimb region mimics by the orientation of the planar anisotropy. The trishear asymmetry angle in the backlimb region of the mechanical model is primarily affected by the orientation of anisotropy.

4. In general, as the magnitude and inclination of the anisotropy increase, the trishear apical angle decreases.

5. The trishear parameters that describe physical models of fault-bend folds with different magnitudes of anisotropy also show a decrease in apical angle with an increase in magnitude of anisotropy. Yet the apical angles of the backlimb of physical models generally are less than these predicted by the mechanical model for the same magnitude of anisotropy. In addition, the physical models display significantly more negative asymmetry than predicted by the mechanical model.

REFERENCES

Allmendinger,R.W., 1998. Inverse and forward numerical modeling of trishear fault-propagation folds. Tectonics 17 (4), 640-656.

Berger, P., Johnson. A.M., 1980. First-order analysis of deformation of a thrust sheet moving over a ramp. Tectonophysics 70, T9-T24.

Berger, P., Johnson, A.M., 1982. Folding of passive layers and forms of minor structures near termination of blind thrust faults–application to the central Appalachian blind thrust. Journal of Structural Geology 4, 343-353.

Biot, M.A., 1965. Further development of the theory of internal bucking of multilayers. Geological Society of America Bulletin 76, 833-840.

Cardozo, N., Bhalla, K., Zehnder, A.T., Allmendinger, R.W., 2003. Mechanical models of fault propagation folds and comparison to the trishear kinematic model. Journal of Structural Geology 25, 1-18.

Chester, J.S., 1985. Deformation of layered rocks in the ramp regions of thrust faults: a study with rock models. MS. Thesis, Texas A&M University, College Station, Texas.

Chester,J.S., 1992. Role of anisotropy on the internal evolution of a thrust sheet. Ph.D. Dissertation,Texas A&M University, College Station, Texas.

Chester, J.S., Fletcher, R.C., 1997. Stress distribution and failure in anisotropic rock near a bend on a weak fault. Journal of Geophysical Research 102 (B1), 693-708.

Chester, J.S., Logan, J.M., Spang, J.H., 1991. Influence of layering and boundary conditions on fault-bend and fault-propagation folding. Geological Society of America Bulletin 103, 1059-1072.

Cristallini, E.O., Allmendinger, R.W., 2001. Pseudo 3-D modeling of trishear fault-propagation folding. Journal of Structural Geology 23, 1883-1899.

Cristallini, E.O., Allmendinger, R.W., 2002. Backlimb trishear: a kinematic model for curved folds developed over angular fault bends. Journal of Structural Geology 24 (2), 289-295.

Erslev, E.A., 1991. Trishear fault-propagation folding. Geology 19, 617-620.

Finch, E., Hardy, S., Gawthorpe, R., 2003. Discrete element modeling of contractional fault-propagation folding above rigid basement fault blocks. Journal of Structural Geology, 25 (4) 515-528.

Hardy, S., Ford, M., 1997. Numerical modeling of trishear fault propagation folding. Tectonics 16 (5), 841-854.

Jamison, W.R., 1987. Geometric analysis of fold development in overthrust terrains. Journal of Structural Geology 9, 207-219.

Johnson, A.M., 1977. Styles of folding. Elsevier, New York.

Johnson, A.M., 1980. Folding and faulting of strain-hardening sedimentary rocks. Tectonophysics 62, 251-278.

Johnson, A.M., Berger, P., 1989. Kinematics of fault-bend folding. Engineering Geology 27, 181-200.

Johnson, A.M., Fletcher, R.C., 1994. Folding of Viscous Layers. Columbia University Press, New York.

Johnson, K.M., Johnson, A.M., 2002a. Mechanical models of trishear-like folds. Journal of Structural Geology 24 (2), 277-287.

Johnson, K.M., Johnson, A.M., 2002b. Mechanical analysis of the geometry of forced-folds. Journal of Structural Geology 24 (3), 401-410.

Kilsdonk, B., Fletcher, R.C., 1989. An analytical model of hanging-wall and footwall deformation at ramps on normal and thrust faults. Tectonophysics 163, 153-168.

Lanczos, C., 1961. Applied Analysis. Prentice-Hall, Englewood Cliffs, New Jersey, pp.225.

Mase, G.E., Mase, G.T., 1992. Continuum Mechanics for Engineers. CRC Press, Boca Raton.

Medwedeff, D.A., 1989. Growth fault-bend folding at Southeast Lost Hills, San Joaquin Valley, California. American Association of Petroleum Geologists Bulletin 73, 54-67.

Medwedeff, D.A., 2000. Review of growth fault-bend folding at SE Lost Hills. American Association of Petroleum Geologists Pacific Section and Western Region Society of Petroleum Engineering Meeting Abstract 84, 884.

Mitra, S., 1990. Fault-propagation folds: Geometry, kinematic evolution, and hydrocarbon traps. American Association of Petroleum Geologists Bulletin 74, 921-945.

Mitra, S., Islam, Q.T., 1994. Experimental (clay) models of inversion structures. Tectonophysics 230, 211-222.

Morse, J., 1977. Deformation in ramp regions of overthrust faults: experiments with small-scale rock models. In: Joint Wyoming-Montana-Utah Geological Association Guidebook. Rocky Mountain Thrust Belt Geology and Resources. 29th Annual Field Conference, Wyoming Geological Association, pp. 457-470.

Morse, J., 1978. Deformation in ramp regions of thrust faults: experiments with rock models. M.S. Thesis,Texas A&M University, College Station, Texas.

Namson, J.S., Davis, T., 1988. Seismically active fold-and-thrust belt in the San Joaquin Valley, central California. Geological Society of America Bulletin 100, 257-273.

Narr, W., Suppe, J., 1994. Kinematics of basement-involved compressive structures. American Journal of Science 294, 802-860.

Patton, T.L., 1984. Normal-fault and fold development in sedimentary rocks above a pre-existing basement normal fault. Ph.D. Dissertation,Texas A&M University, College Station, Texas.

Patton, T.L., Fletcher, R.C., 1998a. Mathematical block-motion model for deformation of a layer above a buried fault of arbitrary dip and sense of slip. Journal of Structural Geology 17 (10), 1455-1472.

Patton, T.L., Fletcher, R.C., 1998b. A rheological model for fractured rock. Journal of Structural Geology 20 (5), 491-502.

Rich, J.L, 1934. Mechanics of low-angle overthrust faulting as illustrated by Cumberland thrust block, Virginia, Kentucky, and Tennessee. Bulletin of the American Association of Petroleum Geologists 18, 1584-1596.

Serra, S., 1977. Styles of deformation in the ramp region of overthrust faults. In: Joint Wyoming-Montana-Utah Geological Association Guidebook. Rocky Mountain Thrust Belt Geology and Resources. 29th Annual Field Conference, Wyoming Geological Association, pp.487-498.

Sherwin, J.A., Chapple, W.M., 1968. Wavelengths of single layer folds: A comparison between theory and observation. American Journal of Science 266, 167-179.

Suppe, J., 1983. Geometry and kinematics of fault-bend folding. American Journal of Science 283, 684-721.

Suppe, J., Medwedeff, D.A., 1990. Geometry and kinematics of fault-propagation folding. Eclogae Geologicae Helvetiae 83, 409-454.

Wiltschko, D.V., 1979a. A mechanical model for thrust sheet deformation at a ramp. Journal of Geophysical Research 84, 1091-1104.

Wiltschko, D.V., 1979b. Partitioning of energy in a thrust sheet and implications concerning driving forces. Journal of Geophysical Research 84, 6050-6058.

Withjack, M.O., Olson, J., and Peterson, E., 1990. Experimental models of extensional forced folds.American Association of Petroleum Geologists Bulletin 74, 1038-1054.

Zehnder, A.T., Allmendinger, R.W., 2000. Velocity field for the trishear model. Journal of Structural Geology 22, 1009-1014.

APPENDIX A

ANALYTICAL SOLUTION OF CHESTER AND FLETCHER (1997)

Model description

The truncated Fourier sine series represent the periodical array of isolated bends:

$$\zeta(x) = \sum_{k=1}^{N} B_k \gamma_k \sin(\lambda_k x) \tag{A.1}$$

where $z = \zeta(x)$ is the normal distance of the sliding surface from the mean plane. λ_k are the wave number of each component in the Fourier series.

The Fourier coefficients are

$$B_k = \frac{2H(\sin[(2k-1)(\pi - W/2)] + \sin[(2k-1)W/2])}{W\pi(2K-1)^2}, \tag{A.2}$$

$$\gamma_k = \frac{\sin[(2k-1)\pi/N]}{[(2k-1)\pi/N]} \tag{A.3}$$

$$\lambda_k = (2k-1)l. \tag{A.4}$$

H is the height from lower flat to upper flat, l is the wave number of each sinusoidal sliding surface. The Gibbs factors, γ_k smooth the truncated Fourier series at discontinuities (Lanczos, 1961). Parameter N describes the angularities of isolated bends. As N increases, ramp is more planar and the bends become sharper as smaller wavelength terms of the Fourier series are added. Three bend geometries are investigated in Chester and Fletcher (1997) and in this study with $N = 10, 32, 100$. The bends are locally rounded with $N = 10$, and sufficiently angular to represent angular bends by $N = 32$ (Chester and Fletcher, 1997).

The coefficient 2 in front of H in the equation (A.2) was incorrectly omitted in Chester and Fletcher (1997) equation (2b). All related calculations herein are based on the corrected equation (A.2).

APPENDIX B

VELOCITY FIELDS IN THE BACKLIMB TRISHEAR

The boundary conditions for backlimb triangular zone within $x' - y'$ coordinate system are:

$$V'_{0x} = V_0 \sin|\lambda_0|\text{sgn}\lambda_0, \quad V'_{0y} = -V_0 \cos|\lambda_0|, \quad \text{for} \;\; y' = x' \tan\varphi,$$

$$V'_{1x} = V_1 \sin|\lambda_1|\text{sgn}\lambda_1, \quad V'_{1y} = -V_1 \cos|\lambda_1|, \quad \text{for} \;\; y' = -x' \tan\varphi. \tag{B.1}$$

V_0 and V_1 are the velocities before and after the fault bend, respectively, given by:

$$V_1 = \frac{V_0 - \Delta V_0 \text{sgn}(\frac{\theta}{2} - \alpha_{ca})}{\cos\theta}$$

where

$$\Delta V_0 = \frac{V_0 \tan\theta \tan(|\frac{\theta}{2} - \alpha_{ca}|)}{1 + [\tan\theta \tan(|\frac{\theta}{2} - \alpha_{ca}|)]}. \tag{B.2}$$

α_{ca} is the asymmetry angle, which is defined to be the angle between bisector of apical angle and bisector of fault bend. 2φ is the apical angle of backlimb triangular zone, θ is the ramp slope of a fault-bend fold. λ_0 represents the angle between lower flat and y' axis. λ_1 represent the angle between fault ramp and y' axis (see Fig. 2.1):

$$\lambda_0 = \alpha_{ca} - \frac{\theta}{2}$$

$$\lambda_1 = \alpha_{ca} + \frac{\theta}{2} \tag{B.3}$$

Cristallini and Allmendinger (2002) assume (1) area conservation within the backlimb triangular zone, and (2) incompressibility flow to derive the velocity field within triangular zone. Condition of flow incompressibility can be specified mathematically (Mase and Mase, 1992; Zehnder and Allmendinger, 2000) as:

$$\text{div}\underline{V'} = \frac{\partial V'_x}{\partial x'} + \frac{\partial V'_y}{\partial y'}. \tag{B.4}$$

A linear but non-unique V'_x field that satisfies these assumptions and boundaries conditions is:

$$V'_x = \frac{V'_{0x}}{2}[\frac{y'}{x' \tan \varphi} + 1] + \frac{V'_{1x}}{2}[\frac{-y'}{x' \tan \varphi} + 1]. \tag{B.5}$$

Then V'_y can be derived by differentiating V'_x with respect x' and integrating with respect to y':

$$V'_y = (V'_{0x} - V'_{1x})[\frac{1}{4 \tan \varphi}(\frac{y'}{x'})^2] + C. \tag{B.6}$$

The integration constant C can be derived using one of the boundary conditions:

$$C = (V'_{1x} - V'_{0x})[\frac{\tan \varphi}{4}] + V'_{0y}. \tag{B.7}$$

APPENDIX C

ALGORITHM OF DEFORMATION GRIDS

An efficient way to investigate the progressive deformation process described by kinematic or mechanical models is to record the displacement of initially orthogonal grids as a result of repeated incremental displacement. In this study, deformation grids are employed to examine fault displacement, fault evolution, layer thickness changes, and folding as predicted by the velocity fields of the mechanical model.

Grid construction and parameters

The deformation grids are constructed and displaced as follows: at any time T_0, a Cartesian grid of user-defined size is superposed on the hanging-wall portion of the fault. The mesh points are labeled (ii, jj) where ii is the vertical side lines counting from the left, $ii = 1, 2, 3 \cdots$; jj is the number of horizontal top lines counting from the base. The same label, (ii, jj) will apply to the elements leading diagonal node (it is called node). The location of each element in global coordinate system is labeled as $(is(ii, jj), js(ii, jj))$. For a simple sinusoidal sliding surface, $-L/2 \leq is \leq L/2; 0 \leq js \leq L$.

Each node is represented as a dot in initial and deformed grids. All elements in the grid are connected by top lines (ii) and side lines (jj) through nodes. If the grid size is small enough, in the limiting case, every particle point can be represented with the node. A square in the grid is comprised of 4 nodes, 2 top lines, and 2 side lines. In this algorithm, timestep is a variable describes the number of iteration, and Δt is the time needed for each iteration. Total time increment equals to the product of Δt and the timestep. The bar lengths between nodes and angles between lines (side line, top line etc) reflect the distortion caused by strain.

Successive displacement

The Cartesian grid is subjected to the motion passing over the fault ramp. Chester and Fletcher (1997) velocity descriptions provide the rate of displacement for a particle at any point of the grid. The velocity description is represented using a vector form as in Fig. 3.3 and Fig. 3.5.

Small displacement to the grid is achieved by adding an increment of time to all nodal points successively. Every element within velocity field will be displaced in the direction of velocity. Mathematically, the displacement is calculated by multiplying time increment Δt to velocity of every node in field. The latest physical position of every node is determined by adding the displacement increment (product of velocity of node and Δt) to the previous position (is, js). The total displacement is achieved by summing all displacements.

Once the largest displacement is achieved, the top lines, side lines, and nodes of final elements are reconstructed to display the final state of the grid.

Source code

```
% This is the deformed grids code for hanging wall deformation
L = 2*pi;
slope = 20;
W = pi/21;
h = W/2*tan(slope*pi/180);
factor = 0.6667;
In =  factor *h;     % increment
m    = 10;
alpha=0;
V = 2;
N = 100;
[w1,w2,v1,v2, A2,A3,B2,B3,b] = norCoeff(m,alpha);
zero = 0;
deltat = 0.15*W;   % time increment
[is,js] = meshgrid( -40*In : In: 20*In, -1.5*In:In:58.5*In);
for timestep = 1:1:20

   for ii = 1:61
      for jj = 1:61
         if js(ii,jj)>=0
            xdisp(ii,jj) = deltat*(Vxfn(is(ii,jj),js(ii,jj),m,
                alpha,w1,w2,v1,v2, A2,A3,B2,B3,b,N,slope)+V/2);
            zdisp(ii,jj) = deltat*Vzfn(is(ii,jj),js(ii,jj), m,
```

```
                alpha,w1,w2,v1,v2, A2,A3,B2,B3,b,N,slope);
         else
            xdisp(ii,jj) = deltat*(Vxfn(is(ii,jj), zero, m,
                alpha,w1,w2,v1,v2, A2,A3,B2,B3,b,N,slope)+V/2);
            zdisp(ii,jj) = deltat*Vzfn(is(ii,jj),zero, m,
                alpha,w1,w2,v1,v2, A2,A3,B2,B3,b,N,slope);
        end
    end
end
is = is + xdisp;
js = js + zdisp;
end
hold on;
plot (is,js,'k-');
hold on;
plot(is',js','k-');
axis image;

%---Plot the ramp----
x = linspace(-L/16,L/6,30);
shapef = 0;
for kk = 1:1:N
   Bk = 2*2*h*(sin((2*kk-1)*(pi-W/2))+
                sin((2*kk-1)*W/2))/(W*pi*(2*kk-1)^2);
   rk = sin((2*kk-1)*pi/N)/((2*kk-1)*pi/N);
   A_pa = Bk*rk;   %A_pa is the amplitude of periodical array
   shapef = shapef +exag_factor*A_pa*sin((2*kk-1)*x);
end
plot (x,shapef,'k');
axis equal;
```

APPENDIX D

SOURCE CODES–VELOCITY SOLUTION

Velocity solution for simple sinusoidal sliding surface

The following source codes call functions $norCoeff$, Vxn, and Vzn.

```
L = 2*pi;  % wavelength
m = 10;
alpha = 22.5;
In = 2 * pi / 20;  % increment
slope = 10;
A = tan(slope*pi/180);  % amplitude
[w1,w2,v1,v2, A2,A3,B2,B3,b] = norCoeff(m,alpha);
[is,js] = meshgrid((-L/2):In:(L/2), 0:In:L);

for ii = 1:(L/In)+1
   for jj = 1:(L/In)+1
     xtemp = Vxn(is(ii,jj),js(ii,jj), m,alpha,w1,w2,v1,v2,
                                              A2,A3,B2,B3,b,A);
     Pxn(ii,jj) = xtemp;
     ztemp = Vzn(is(ii,jj),js(ii,jj), m,alpha,w1,w2,v1,v2,
                                             A2,A3,B2,B3,b,A);
     Pzn(ii,jj) = ztemp;
  end
end

quiver(is,js,Pxn,Pzn,1.3);
axis image;
```

Functions

Function Vxn:

```
function r = Vxn(x,z,m,alpha,w1,w2,v1,v2, A2,A3,B2,B3,b,A)
% ------------------------------------------------
% normalized velocity function (Vx)for sinusoidal surface
% when z>=0.
%------------------------------------------------
V = 2;
alpha1 = alpha*pi/180;
norfactor = V*A/2;

k1  = ((1+m)+(1-m)*cos(4*alpha1))*norfactor/(4*m^0.5);
k2  = (A2*(v1^2-w1^2-1)+B2*(-2*w1*v1))*sin(v1*z);
k3  = (A2*(2*w1*v1)+B2*(v1^2-w1^2-1))*cos(v1*z);
k4  = (A3*(v2^2-w2^2-1)+B3*(2*w2*v2))*sin(v2*z);
k5  = (A3*(-2*w2*v2)+B3*(v2^2-w2^2-1))*cos(v2*z);
k6  = (A2*(v1^2-w1^2-1)+B2*(-2*w1*v1))*cos(v1*z);
k7  = (A2*(-2*w1*v1)+B2*(1+w1^2-v1^2))*sin(v1*z);
k8  = (A3*(v2^2-w2^2-1)+B3*(2*w2*v2))*cos(v2*z);
k9  = (A3*(2*w2*v2)+B3*(1+w2^2-v2^2))*sin(v2*z);
k10 = (-A2*w1-B2*v1)*cos(v1*z);
k11 = (-A2*v1+B2*w1)*sin(v1*z);
k12 = (A3*w2-B3*v2)*cos(v2*z);
k13 = (-A3*v2-B3*w2)*sin(v2*z);
k14 = (-A2*v1+B2*w1)*cos(v1*z);
k15 = (A2*w1+B2*v1)*sin(v1*z);
k16 = (-A3*v2-B3*w2)*cos(v2*z);
k17 = (-A3*w2+B3*v2)*sin(v2*z);

r1  = ((k2+k3)*exp(-w1*z)+(k4+k5)*exp(w2*z))*cos(x);
r2  = ((k6+k7)*exp(-w1*z)+(k8+k9)*exp(w2*z))*sin(x);
r3  = 2*b*((k10+k11)*exp(-w1*z)+(k12+k13)*exp(w2*z))*cos(x);
r4  = 2*b*((k14+k15)*exp(-w1*z)+(k16+k17)*exp(w2*z))*sin(x);
r   = k1*(r1+r2+r3+r4);
```

Function Vzn:

```
function rz=Vzn(x,z,m,alpha,w1,w2,v1,v2, A2,A3,B2,B3,b,A)
 % ------------------------------------------------
% normalized velocity function (Vz)for sinusoidal surface
% when z>=0.
%-------------------------------------------------
V = 2;
alpha1 = alpha*pi/180;
norfactor = V*A/2;

j1  = ((1+m)+(1-m)*cos(4*alpha1))*norfactor/(4*m^0.5);
j2  = (-w1*(1+w1^2+v1^2)*cos(v1*z));
j3  = (-v1*(-1+w1^2+v1^2)*sin(v1*z));
j4  = (-v1*(-1+w1^2+v1^2)*cos(v1*z));
j5  = (w1*(1+w1^2+v1^2)*sin(v1*z));
j6  = (w2*(1+w2^2+v2^2)*cos(v2*z));
j7  = (-v2*(-1+w2^2+v2^2)*sin(v2*z));
j8  = (-v2*(-1+w2^2+v2^2)*cos(v2*z));
j9  = (-w2*(1+w2^2+v2^2)*sin(v2*z));
j10 = (-v1*(-1+w1^2+v1^2)*cos(v1*z));
j11 = (w1*(1+w1^2+v1^2)*sin(v1*z));
j12 = (w1*(1+w1^2+v1^2)*cos(v1*z));
j13 = (v1*(-1+w1^2+v1^2)*sin(v1*z));
j14 = (-v2*(-1+w2^2+v2^2)*cos(v2*z));
j15 = (-w2*(1+w2^2+v2^2)*sin(v2*z));
j16 = (-w2*(1+w2^2+v2^2)*cos(v2*z));
j17 = (v2*(-1+w2^2+v2^2)*sin(v2*z));

rz1 = j1*((A2*(j2+j3)+B2*(j4+j5))*(exp(-w1*z)/(w1^2+v1^2))+
     (A3*(j6+j7)+B3*(j8+j9))*(exp(w2*z)/(w2^2+v2^2))+
     2*b*((A2*sin(v1*z)+B2*cos(v1*z))*exp(-w1*z)+
     (A3*sin(v2*z)+B3*cos(v2*z))*exp(w2*z)))*cos(x);
```

```
rz2 = j1*((A2*(j10+j11)+B2*(j12+j13))*(exp(-w1*z)/(w1^2+v1^2))+
     (A3*(j14+j15)+B3*(j16+j17))*(exp(w2*z)/(w2^2+v2^2))+
     2*b*((A2*cos(v1*z)-B2*sin(v1*z))*exp(-w1*z)+
     (A3*cos(v2*z)-B3*sin(v2*z))*exp(w2*z)))*sin(x);
rz = rz1+rz2;

Function norCoeff:

function [w1,w2,v1,v2, A2,A3,B2,B3,b]=norCoeff(m,alpha)
% Function of normalized constants
alpha1 = alpha*pi/180;
a = ((1+m)-(1-m)*cos(4*alpha1))/((1+m)+(1-m)*cos(4*alpha1));
b = ((1-m)*sin(4*alpha1))/((1+m)+(1-m)*cos(4*alpha1));

C = (2*(m-1)*(1+cos(4*alpha1)))^0.5/((1+m)+(1-m)*cos(4*alpha1));
R = 2*m^0.5/((1+m)+(1-m)*cos(4*alpha1));

w1 = (C+R);
w2 = (C-R);
v1 = b*(1+R/C);
v2 = b*(1-R/C);

z31 = (-w1)*(1+w1^2+v1^2)/(w1^2+v1^2);
z32 = w2*(1+w2^2+v2^2)/(w2^2+v2^2);
z33 = 2*b+(-v1)*(-1+w1^2+v1^2)/(w1^2+v1^2);
z34 = 2*b+(-v2)*(-1+w2^2+v2^2)/(w2^2+v2^2);

z41 = 2*b+(-v1)*(-1+w1^2+v1^2)/(w1^2+v1^2);
z42 = 2*b+(-v2)*(-1+w2^2+v2^2)/(w2^2+v2^2);
z43 = w1*(1+w1^2+v1^2)/(w1^2+v1^2);
z44 = (-w2)*(1+w2^2+v2^2)/(w2^2+v2^2);

tmp=[v1 v2 -w1 w2; w1 -w2 v1 v2; z31 z32 z33 z34; z41 z42 z43 z44];
```

```
D31 = 4*m^0.5/((1+m)+(1-m)*cos(4*alpha1));

y = tmp^-1*[0;0;D31;0];
A2=y(1); A3=y(2); B2=y(3); B3=y(4);
```

Velocity solution for isolate bends

The following source codes call functions $norCoeff$, $Vxfn$, and $Vzfn$.

```
L = 2 * pi;            %wavelength
m = 10;
alpha = 20;
In = 2 * pi / 20;     % increment
slope = 10;
N = 100;
[w1,w2,v1,v2, A2,A3,B2,B3,b] = norCoeff (m,alpha);

[is,js] = meshgrid((-L/2):In:(L/2),0:In:L);

for ii = 1:21
   for jj = 1:21
      xtemp = Vxfn(is(ii,jj),js(ii,jj), m,alpha,w1,
                              w2,v1,v2, A2,A3,B2,B3,b,N,slope);
      Pxf(ii,jj) = xtemp;
      ztemp = Vzfn(is(ii,jj),js(ii,jj), m,alpha,w1,
                              w2,v1,v2, A2,A3,B2,B3,b,N,slope);
      Pzf(ii,jj) = ztemp;
   end
end
quiver(is,js,Pxf,Pzf,1.3);
axis image;

Function Vxfn:
```

```
function rf=Vxfn(x,z,m,alpha,w1,w2,v1,v2, A2,A3,B2,B3,b,N,slope)
% ------------------------------------------------
% normalized velocity function (Vx)for Periodical arrays
% when z>=0.
%-------------------------------------------------
V = 2;
alpha1 = alpha*pi/180;
W = pi/21;
% 2h is the height from crest to trough of isolated ramp.
h = W*tan(slope*pi/180)/2;
rf = 0;
for kk = 1:N
    Bk = 2*2*h*(sin((2*kk-1)*(pi-W/2))+
                  sin((2*kk-1)*W/2))/(W*pi*(2*kk-1)^2);
    rk = sin((2*kk-1)*pi/N)/((2*kk-1)*pi/N);
    norfactor = Bk*rk*(2*kk-1)*V/2;
    k1  = ((1+m)+(1-m)*cos(4*alpha1))*norfactor/(4*m^0.5);
    k2  = (A2*(v1^2-w1^2-1)+B2*(-2*w1*v1))*sin(v1*(2*kk-1)*z);
    k3  = (A2*(2*w1*v1)+B2*(v1^2-w1^2-1))*cos(v1*(2*kk-1)*z);
    k4  = (A3*(v2^2-w2^2-1)+B3*(2*w2*v2))*sin(v2*(2*kk-1)*z);
    k5  = (A3*(-2*w2*v2)+B3*(v2^2-w2^2-1))*cos(v2*(2*kk-1)*z);
    k6  = (A2*(v1^2-w1^2-1)+B2*(-2*w1*v1))*cos(v1*(2*kk-1)*z);
    k7  = (A2*(-2*w1*v1)+B2*(1+w1^2-v1^2))*sin(v1*(2*kk-1)*z);
    k8  = (A3*(v2^2-w2^2-1)+B3*(2*w2*v2))*cos(v2*(2*kk-1)*z);
    k9  = (A3*(2*w2*v2)+B3*(1+w2^2-v2^2))*sin(v2*(2*kk-1)*z);
    k10 = (-A2*w1-B2*v1)*cos(v1*(2*kk-1)*z);
    k11 = (-A2*v1+B2*w1)*sin(v1*(2*kk-1)*z);
    k12 = (A3*w2-B3*v2)*cos(v2*(2*kk-1)*z);
    k13 = (-A3*v2-B3*w2)*sin(v2*(2*kk-1)*z);
    k14 = (-A2*v1+B2*w1)*cos(v1*(2*kk-1)*z);
    k15 = (A2*w1+B2*v1)*sin(v1*(2*kk-1)*z);
    k16 = (-A3*v2-B3*w2)*cos(v2*(2*kk-1)*z);
    k17 = (-A3*w2+B3*v2)*sin(v2*(2*kk-1)*z);
    r1 = ((k2+k3)*exp(-w1*(2*kk-1)*z)+
```

```
                (k4+k5)*exp(w2*(2*kk-1)*z))*cos((2*kk-1)*x);
    r2 = ((k6+k7)*exp(-w1*(2*kk-1)*z)+
                (k8+k9)*exp(w2*(2*kk-1)*z))*sin((2*kk-1)*x);
    r3 = 2*b*((k10+k11)*exp(-w1*(2*kk-1)*z)+
                (k12+k13)*exp(w2*(2*kk-1)*z))*cos((2*kk-1)*x);
    r4 = 2*b*((k14+k15)*exp(-w1*(2*kk-1)*z)+
                (k16+k17)*exp(w2*(2*kk-1)*z))*sin((2*kk-1)*x);
    rf = rf+temp_x;
end
```

Function Vzfn:

```
function rzf=Vzfn(x,z,m,alpha,w1,w2,v1,v2, A2,A3,B2,B3,b,N,slope)
% ------------------------------------------------
% normalized velocity function (Vz)for Periodical arrays
% when z>=0.
%------------------------------------------------
V = 2;
alpha1 = alpha*pi/180;
W = pi/21;
% 2h is the height from crest to trough of isolated ramp.
h = W*tan(slope*pi/180)/2;
rzf = 0;
for kk = 1:N
    Bk = 2*2*h*(sin((2*kk-1)*(pi-W/2))+
                 sin((2*kk-1)*W/2))/(W*pi*(2*kk-1)^2);
    rk = sin((2*kk-1)*pi/N)/((2*kk-1)*pi/N);
    norfactor = Bk*rk*(2*kk-1)*V/2;

    j1  = ((1+m)+(1-m)*cos(4*alpha1))*norfactor/(4*m^0.5);
    j2  = (-w1*(1+w1^2+v1^2)*cos(v1*(2*kk-1)*z));
    j3  = (-v1*(-1+w1^2+v1^2)*sin(v1*(2*kk-1)*z));
    j4  = (-v1*(-1+w1^2+v1^2)*cos(v1*(2*kk-1)*z));
    j5  = (w1*(1+w1^2+v1^2)*sin(v1*(2*kk-1)*z));
```

```
    j6  = (w2*(1+w2^2+v2^2)*cos(v2*(2*kk-1)*z));
    j7  = (-v2*(-1+w2^2+v2^2)*sin(v2*(2*kk-1)*z));
    j8  = (-v2*(-1+w2^2+v2^2)*cos(v2*(2*kk-1)*z));
    j9  = (-w2*(1+w2^2+v2^2)*sin(v2*(2*kk-1)*z));
    j10 = (-v1*(-1+w1^2+v1^2)*cos(v1*(2*kk-1)*z));
    j11 = (w1*(1+w1^2+v1^2)*sin(v1*(2*kk-1)*z));
    j12 = (w1*(1+w1^2+v1^2)*cos(v1*(2*kk-1)*z));
    j13 = (v1*(-1+w1^2+v1^2)*sin(v1*(2*kk-1)*z));
    j14 = (-v2*(-1+w2^2+v2^2)*cos(v2*(2*kk-1)*z));
    j15 = (-w2*(1+w2^2+v2^2)*sin(v2*(2*kk-1)*z));
    j16 = (-w2*(1+w2^2+v2^2)*cos(v2*(2*kk-1)*z));
    j17 = (v2*(-1+w2^2+v2^2)*sin(v2*(2*kk-1)*z));
    rz1 = j1*((A2*(j2+j3)+B2*(j4+j5))*(exp(-w1*(2*kk-1)*z)/(w1^2
          +v1^2))+(A3*(j6+j7)+B3*(j8+j9))*(exp(w2*(2*kk-1)*z)/(w2^2+
          v2^2))+2*b*((A2*sin(v1*(2*kk-1)*z)+B2*cos(v1*(2*kk-1)*z))*
          exp(-w1*(2*kk-1)*z)+(A3*sin(v2*(2*kk-1)*z)+B3*cos(v2*
          (2*kk-1)*z))*exp(w2*(2*kk-1)*z)))*cos((2*kk-1)*x);
    rz2 = j1*((A2*(j10+j11)+B2*(j12+j13))*(exp(-w1*(2*kk-1)*z)/(w1^2
          +v1^2))+(A3*(j14+j15)+B3*(j16+j17))*(exp(w2*(2*kk-1)*z
          )/(w2^2+v2^2))+2*b*((A2*cos(v1*(2*kk-1)*z)-B2*
          sin(v1*(2*kk-1)*z))*exp(-w1*(2*kk-1)*z)+(A3*cos(v2*
          (2*kk-1)*z)-B3*sin(v2*(2*kk-1)*z))*exp(w2*(2*kk-1)*z)))
          *sin((2*kk-1)*x);
    temp_z=rz1+rz2;
    rzf=rzf+temp_z;
end
```

APPENDIX E

SOURCE CODES–STRESS SOLUTION

Stress solution for simple sinusoidal sliding surface

The following Matlab code calls functions $norCoeff$, $sigmaxxs$,$sigmaxzs$, and $sigmazzs$.

```
L = 2*pi;
In = 2*pi/60;
m = 10;
alpha = 22.5;
slope = 10;
A = tan(slope*pi/180);
mag = 1; %magnification factor
[w1,w2,v1,v2, A2,A3,B2,B3,b] = norCoeff(m,alpha);
[is,js] = meshgrid(-L/2:In:L/2, 0:In:L);
for ii = 1:1:(L/In+1)
   for jj = 1:1:(L/In+1)
      stressx(ii,jj) = sigmaxxs(is(ii,jj),js(ii,jj),w1,w2,
v1,v2, A2,A3,B2,B3);
      stressz(ii,jj) = sigmazzs(is(ii,jj),js(ii,jj),w1,w2,
v1,v2, A2,A3,B2,B3);
      stressxz(ii,jj)= sigmaxzs(is(ii,jj),js(ii,jj),w1,w2,
v1,v2, A2,A3,B2,B3);
      stress=[stressx(ii,jj) stressxz(ii,jj);
stressxz(ii,jj) stressz(ii,jj)];
      [vectors principal]=eig(stress);
      sigma1=principal(1,1)*vectors(:,1)*mag;
      sigma3=principal(2,2)*vectors(:,2)*mag;
     Meanstress(ii,jj)=(principal(1,1)+principal(2,2))/2;
     Dev_stress(ii,jj)=(principal(2,2)-principal(1,1))/2;
```

```
   end
end
axis image;
[cc,hh]= contourf(is,js,Meanstress,9);clabel(cc,hh);
axis image;
```

Stress Functions of sinusoidal sliding surface

Function sigmaxxs:

```
function normalx = sigmaxxs(x,z,w1,w2,v1,v2, A2,A3,B2,B3)
%normalized perturbing stress of acting on the x direction
xx1 = (A2*((v1^2-w1^2)*cos(v1*z)-2*w1*v1*sin(v1*z))+
      B2*(-2*w1*v1*cos(v1*z)-(v1^2-w1^2)*sin(v1*z)))*
      exp(-w1*z);
xx2 = (A3*((v2^2-w2^2)*cos(v2*z)+2*w2*v2*sin(v2*z))+
      B3*(2*w2*v2*cos(v2*z)-(v2^2-w2^2)*sin(v2*z)))*
      exp(w2*z);
xx3 = (A2*(-2*w1*v1*cos(v1*z)-(v1^2-w1^2)*sin(v1*z))+
      B2*(-(v1^2-w1^2)*cos(v1*z)+2*w1*v1*sin(v1*z)))*
      exp(-w1*z);
xx4 = (A3*(2*w2*v2*cos(v2*z)-(v2^2-w2^2)*sin(v2*z))+
      B3*(-(v2^2-w2^2)*cos(v2*z)-2*w2*v2*sin(v2*z)))*
      exp(w2*z);
normalx = (xx1+xx2)*cos(x)+(xx3+xx4)*sin(x);
```

Function sigmaxzs:

```
function shearstress=sigmaxzs(x,z,w1,w2,v1,v2, A2,A3,B2,B3)
% function: normalized perturbing shear stress
if z==0
    shearstress=0;
else
```

```
xz1 = (A2*(-v1*cos(v1*z)+w1*sin(v1*z))+
       B2*(w1*cos(v1*z)+v1*sin(v1*z)))*exp(-w1*z);
xz2 = (A3*(-v2*cos(v2*z)-w2*sin(v2*z))+
       B3*(-w2*cos(v2*z)+v2*sin(v2*z)))*exp(w2*z);
xz3 = (A2*(w1*cos(v1*z)+v1*sin(v1*z))+
      B2*(v1*cos(v1*z)-w1*sin(v1*z)))*exp(-w1*z);
xz4 = (A3*(-w2*cos(v2*z)+v2*sin(v2*z))+
      B3*(v2*cos(v2*z)+w2*sin(v2*z)))*exp(w2*z);
shearstress = (xz1+xz2)*cos(x)+(xz3+xz4)*sin(x);
end
```

Function sigmazzs:

```
function normalz = sigmazzs(x,z,w1,w2,v1,v2, A2,A3,B2,B3)
% function: normalized perturbing stress acting on the z direction
zz1 = (A2*cos(v1*z)-B2*sin(v1*z))*exp(-w1*z);
zz2 = (A3*cos(v2*z)-B3*sin(v2*z))*exp(w2*z);
zz3 = (A2*sin(v1*z)+B2*cos(v1*z))*exp(-w1*z);
zz4 = (A3*sin(v2*z)+B3*cos(v2*z))*exp(w2*z);
normalz = (zz1+zz2)*cos(x)-(zz3+zz4)*sin(x);
```

Stress solution for isolated bends

The following Matlab code calls functions $norCoeff$, $sigmaxn$,$sigmaxzn$, and $sigmazzn$.

```
L    = 2*pi;
In   = 2*pi/(60*16);
m    = 10;
alpha = 22.5;
N    = 32;
slope =10;
W = pi/21;
h = W*tan(slope*pi/180)/2;   % 2h is ramp height
```

```
% Call normalized constants function
 [w1,w2,v1,v2, A2,A3,B2,B3,b] = norCoeff(m,alpha);
[is,js]= meshgrid(-L/32:In:L/32, 0:In:L/16);
for ii = 1:1:61,
   for jj = 1:1:61,
      stressx(ii,jj) = sigmaxxn(is(ii,jj),js(ii,jj),w1,w2,
v1,v2, A2,A3,B2,B3,N,h);
      stressz(ii,jj) = sigmazzn(is(ii,jj),js(ii,jj),w1,w2,
v1,v2, A2,A3,B2,B3,N,h);
      stressxz(ii,jj)= sigmaxzn(is(ii,jj),js(ii,jj),w1,w2,
v1,v2, A2,A3,B2,B3,N,h);
      stress = [stressx(ii,jj) stressxz(ii,jj);
stressxz(ii,jj) stressz(ii,jj)];
      [vectors principal] = eig(stress);  %eigenvector
      Meanstress(ii,jj) = (principal(1,1)+principal(2,2))/(2);
      Dev_stress(ii,jj) = (principal(2,2)-principal(1,1))/(2);
   end
end
[cc,hh] = contourf(is,js,Meanstress,9);clabel(cc,hh);
```

Stress Functions for isolated bends

Function sigmaxxn:

```
function normalxn = sigmaxxn(x,z,w1,w2,v1,v2, A2,A3,B2,B3, N,h)
% normalized perturbing stress of PERIODICAL ARRAYS
  acting on the x direction
W = pi/21;
normalxn = 0;
for kk = 1:N
Bk = 2*2*h*(sin((2*kk-1)*(pi-W/2))+
     sin((2*kk-1)*W/2))/(W*pi*(2*kk-1)^2);
rk = sin((2*kk-1)*pi/N)/((2*kk-1)*pi/N);
% normalization factor
```

```
norfactor = 2*(sin((2*kk-1)*(pi-W/2))+
                    sin((2*kk-1)*W/2))/(W*pi)*rk;
A20 = A2*norfactor;
A30 = A3*norfactor;
B20 = B2*norfactor;
B30 = B3*norfactor;
xx1 = (A20*((v1^2-w1^2)*cos(v1*(2*kk-1)*z)-2*w1*v1*
      sin(v1*(2*kk-1)*z))+B20*(-2*w1*v1*cos(v1*(2*kk-1)*z)
      -(v1^2-w1^2)*sin(v1*(2*kk-1)*z)))*exp(-w1*(2*kk-1)*z);
xx2 = (A30*((v2^2-w2^2)*cos(v2*(2*kk-1)*z)+2*w2*v2*
      sin(v2*(2*kk-1)*z))+B30*(2*w2*v2*cos(v2*(2*kk-1)*z)
      -(v2^2-w2^2)*sin(v2*(2*kk-1)*z)))*exp(w2*(2*kk-1)*z);
xx3 = (A20*(-2*w1*v1*cos(v1*(2*kk-1)*z)-(v1^2-w1^2)*
      sin(v1*(2*kk-1)*z))+B20*(-(v1^2-w1^2)*cos(v1*(2*kk-1)*z)
      +2*w1*v1*sin(v1*(2*kk-1)*z)))*exp(-w1*(2*kk-1)*z);
xx4 = (A30*(2*w2*v2*cos(v2*(2*kk-1)*z)-(v2^2-w2^2)*
      sin(v2*(2*kk-1)*z))+B30*(-(v2^2-w2^2)*cos(v2*(2*kk-1)*z)
      -2*w2*v2*sin(v2*(2*kk-1)*z)))*exp(w2*(2*kk-1)*z);
temp_xx(kk) = (xx1+xx2)*cos((2*kk-1)*x)+(xx3+xx4)*sin((2*kk-1)*x);
normalxn = normalxn+temp_xx(kk);
end
```

Function sigmaxzn:

```
function shearstressn=sigmaxzn(x,z,w1,w2,v1,v2, A2,A3,B2,B3,N,h)
% function: total shear stress of PERIODICAL ARRAYS
if z~=0
W = pi/21;
shearstressn = 0;
for kk = 1:N,
   Bk = 2*2*h*(sin((2*kk-1)*(pi-W/2))+
                    sin((2*kk-1)*W/2))/(W*pi*(2*kk-1)^2);
   rk = sin((2*kk-1)*pi/N)/((2*kk-1)*pi/N);
```

```
   norfactor=2*(sin((2*kk-1)*(pi-W/2))+
                   sin((2*kk-1)*W/2))/(W*pi) *rk;
   A20 = A2*norfactor;
   A30 = A3*norfactor;
   B20 = B2*norfactor;
   B30 = B3*norfactor;
   xz1 = (A20*(-v1*cos(v1*(2*kk-1)*z)+w1*sin(v1*(2*kk-1)*z))+
            B20*(w1*cos(v1*(2*kk-1)*z)+v1*sin(v1*(2*kk-1)*z)))*
            exp(-w1*(2*kk-1)*z);
   xz2 = (A30*(-v2*cos(v2*(2*kk-1)*z)-w2*sin(v2*(2*kk-1)*z))+
            B30*(-w2*cos(v2*(2*kk-1)*z)+v2*sin(v2*(2*kk-1)*z)))*
            exp(w2*(2*kk-1)*z);
   xz3 = (A20*(w1*cos(v1*(2*kk-1)*z)+v1*sin(v1*(2*kk-1)*z))+
            B20*(v1*cos(v1*(2*kk-1)*z)-w1*sin(v1*(2*kk-1)*z)))*
            exp(-w1*(2*kk-1)*z);
   xz4 = (A30*(-w2*cos(v2*(2*kk-1)*z)+v2*sin(v2*(2*kk-1)*z))+
            B30*(v2*cos(v2*(2*kk-1)*z)+w2*sin(v2*(2*kk-1)*z)))*
            exp(w2*(2*kk-1)*z);
   temp_xz = (xz1+xz2)*cos((2*kk-1)*x)+(xz3+xz4)*sin((2*kk-1)*x);

shearstressn = shearstressn+temp_xz;
end
else
    shearstressn=0;
end

Function sigmazzn:

function normalzn = sigmazzn(x,z,w1,w2,v1,v2, A2,A3,B2,B3,N,h)
% function: total tress of PERIODICAL ARRAYS
  acting on the z direction
W = pi/21;
normalzn = 0;
for kk = 1:N,
```

```
    Bk = 2*2*h*(sin((2*kk-1)*(pi-W/2))+
                sin((2*kk-1)*W/2))/(W*pi*(2*kk-1)^2);
    rk = sin((2*kk-1)*pi/N)/((2*kk-1)*pi/N);
    norfactor=2*(sin((2*kk-1)*(pi-W/2))+
                    sin((2*kk-1)*W/2))/(W*pi) *rk;
    A20 = A2*norfactor;
    A30 = A3*norfactor;
    B20 = B2*norfactor;
    B30 = B3*norfactor;
    zz1 = (A20*cos(v1*(2*kk-1)*z)-B20*sin(v1*(2*kk-1)*z))*
            exp(-w1*(2*kk-1)*z);
    zz2 = (A30*cos(v2*(2*kk-1)*z)-B30*sin(v2*(2*kk-1)*z))*
            exp(w2*(2*kk-1)*z);
    zz3 = (A20*sin(v1*(2*kk-1)*z)+B20*cos(v1*(2*kk-1)*z))*
            exp(-w1*(2*kk-1)*z);
    zz4 = (A30*sin(v2*(2*kk-1)*z)+B30*cos(v2*(2*kk-1)*z))*
            exp(w2*(2*kk-1)*z);
    temp_zz = (zz1+zz2)*cos((2*kk-1)*x)-(zz3+zz4)*sin((2*kk-1)*x);
    normalzn = normalzn + temp_zz;
end
```

APPENDIX F

MODIFIED STRESS CODE

The following Matlab source code is based on original Quick Basic source code written by Judith Chester.

```
% anisotropic viscous fault model for
  isolated bend solution for stresses
NE = 4;
GS = 61;      %GS must be an odd integer
TH = 10;    %max slope
IRR = 0 ;   %Constraining bend (0) or Releasing bend (1)
VC = 10;    % m
AA = 22.5;  % orientation
NN = 32;    % number of Fourier series
N = NN*2;
M = 16;     % range of x-z plot. - to + (PI/Range)
% function for coefficient equations
TR = TH*pi/180;
AR = AA*pi/180;
AM = tan (TR);
H = AM*pi/42;
D0 = 1+VC + (1-VC)*cos(4*AR);
BB = (1-VC)*sin(4*AR)/D0;
R1 = 2*VC^0.5/D0;
CC = (2*(VC-1)*(1+cos(4*AR)))^0.5/D0;
W1 = CC+R1;
W2 = CC - R1;
V1 = BB + BB*R1/CC;
V2 = BB - BB*R1/CC;
D1 = W1^2 + V1^2;
D2 = W2^2 + V2^2;
A11 = V1;
```

```
A12 = V2;
A13 = -W1;
A14 = W2;
A21 = W1;
A22 = -W2;
A23 = V1;
A24 = V2;
A31 = W1*(-1 - D1)/D1;
A32 = W2*(1 + D2)/D2;
A33 = V1*(1 - D1)/D1 + 2*BB;
A34 = V2*(1 - D2)/D2 + 2*BB;
A41 = A33;
A42 = A34;
A43 = -A31;
A44 = -A32;
Z1 = 0;
Z2 = 0;
Z3 = 4*(VC)^0.5/D0;    % equations written for A2', A3', B2', B3'
Z4 = 0;
tmp = [V1 V2 -W1 W2; W1 -W2 V1 V2;A31 A32 A33 A34;A41 A42 A43 A44];
C1 = tmp^-1*[0;0;Z3;0];
A2 = C1(1); A3 = C1(2);
B2 = C1(3); B3 = C1(4);
%Determine deviatoric stress
%Stress is normalized by 2(normvisc)(Vl)(hl)/sqr(m)
%Stress is unnormalized for summing fourier series, then renormalized
for K = 1: NN
      BK(K)= AM*(sin(K*41*pi/42)+sin(K*pi/42))/(pi*K*K);
      GK(K)= sin(K*pi/NN)/(K*pi/NN);
end
VW1 = V1^2 - W1^2;
VW2 = V2^2 - W2^2;
WV1 = 2*W1*V1;
WV2 = 2*W2*V2;
```

```
DV = GS - 1;
for I = DV+1:-1:1
   for J = 1: DV+1
    GXX(J,I)=0;
    GZZ(J,I)=0;
    GXZ(J,I)=0;
      for K=1:2:N
      ZZ = K*((I-1)*2*(pi/M)/DV);
      XX = K*(((J-1)*2*(pi/M)/DV-(pi/M))+IRR*pi);
      CV1 = cos(V1*ZZ);
      CV2 = cos(V2*ZZ);
      SV1 = sin(V1*ZZ);
      SV2 = sin(V2*ZZ);
      EP1 = exp(-W1*ZZ);
      EP2 = exp(W2*ZZ);
      CX = cos(XX);
      SX = sin(XX);
      GXX1 = C1(1)*(VW1*CV1 - WV1*SV1) + C1(3)*(-WV1*CV1 - VW1*SV1);
      GXX2 = C1(2)*(VW2*CV2 + WV2*SV2) + C1(4)*(WV2*CV2 - VW2*SV2);
      GXX3 = C1(1)*(-WV1*CV1 - VW1*SV1) + C1(3)*(-VW1*CV1 + WV1*SV1);
      GXX4 = C1(2)*(WV2*CV2 - VW2*SV2) + C1(4)*(-VW2*CV2 - WV2*SV2);
      GXXN = (GXX1*EP1 + GXX2*EP2)*CX + (GXX3*EP1 + GXX4*EP2)*SX;
      GZZ1 = C1(1)*CV1 - C1(3)*SV1;
      GZZ2 = C1(2)*CV2 - C1(4)*SV2;
      GZZ3 = C1(1)*SV1 + C1(3)*CV1;
      GZZ4 = C1(2)*SV2 + C1(4)*CV2;
      GZZN = (GZZ1*EP1 + GZZ2*EP2)*CX - (GZZ3*EP1 + GZZ4*EP2)*SX;
      GXZ1 = C1(1)*(W1*CV1 + V1*SV1) + C1(3)*(V1*CV1 - W1*SV1);
      GXZ2 = C1(2)*(-W2*CV2 + V2*SV2) + C1(4)*(V2*CV2 + W2*SV2);
      GXZ3 = C1(1)*(-V1*CV1 + W1*SV1) + C1(3)*(W1*CV1 + V1*SV1);
      GXZ4 = C1(2)*(-V2*CV2 -W2*SV2) + C1(4)*(-W2*CV2 + V2*SV2);
      GXZN = (GXZ1*EP1 + GXZ2*EP2)*SX + (GXZ3*EP1 + GXZ4*EP2)*CX;
      GXZN = GXZN*BK(K)*GK(K)*K*K;
      GXXN = GXXN*BK(K)*GK(K)*K*K;
```

```
      GZZN = GZZN*BK(K)*GK(K)*K*K;
      GXZ(J,I) = GXZN + GXZ(J,I);
      GXX(J,I) = GXXN + GXX(J,I);
      GZZ(J,I)= GZZN + GZZ(J,I);
      end
    GXZ(J,I) = GXZ(J,I)/H;
    GXX(J,I) = GXX(J,I)/H;
    GZZ(J,I) = GZZ(J,I)/H;
    %delete (/(2*pi)) from original code
    ZN(J,I) = ((I-1)*2*(pi/M)/DV);
    %delete (/(2*pi)) from original code
    XN(J,I) = (((J-1)*2*(pi/M)/DV-(pi/M))+IRR*pi);
    end
end
% Plot mean stress & Deviatoric stress
  for I = DV+1:-1: 1
       for J = 1:DV+1
           PR = ((GZZ(J,I) - GXX(J,I))^2/4 + GXZ(J,I)^2)^0.5;
           PS1 = (GZZ(J,I) + GXX(J,I))/2 - PR;
           PS3 = (GXX(J,I) + GZZ(J,I))/2 + PR;
           GM(J,I) = (PS1 + PS3)/2;
           GD(J,I) = abs((PS1 - PS3)/2);
       end
  end

[cc,hh] = contourf(XN,ZN,GM,9);clabel(cc,hh);
axis image;
[cc,hh] = contourf(XN,ZN,GM,9);clabel(cc,hh);
```

APPENDIX G

SOURCE CODE–β CONTOUR FOR THE MECHANICAL MODEL

The following source code calculates the angle β between trishear bisector and velocity vectors in the backlimb region of a Chester and Fletcher (1997) mechanical model.

```
L = 2*pi;
m = 10;
alpha = 20;
In = 2*L/(28*20*4); %increment
slope = 20;
N = 100;
W = pi/21;
h = W/2*tan(slope*pi/180);
[w1,w2,v1,v2, A2,A3,B2,B3,b] = norCoeff(m,alpha);
V = 2;
zero = 0;
% V0 is the velocity at (-pi/4,0)
V0x_p = 0;
V0x_t = V0x_p + V/2;   % basic flow is constantly equal to V/2
V0z_t = 0;
% V1 is the velocity at (0,0)
V1x_p = Vxfn_po(0,0,m,alpha,w1,w2,v1,v2, A2,A3,B2,B3,b,N,slope);
V1x_t = V1x_p + V/2;
V1z_t = Vzfn_po(0,0,m,alpha,w1,w2,v1,v2, A2,A3,B2,B3,b,N,slope);
%  Reference Velocity VR=(V0+V1)/2;
VRx = (V0x_t + V1x_t)/2;
VRz = (V0z_t + V1z_t)/2;
abVR = sqrt(VRx^2 + VRz^2);    % absolute value of vector VR
VR_or=atan(VRz/VRx)*180/pi;   %The orientation of VR in angle
%%%%%%%%%%%%%%%%%%%%%%%%%%%%%%
[is,js] = meshgrid((-L/28):In:(L/28),-h:In:(2*L/28-h));
```

```
for ii = 1:81
  for jj = 1:81
     if js(ii,jj)>=0
     Vx_p(ii,jj) = Vxfn_po(is(ii,jj),js(ii,jj), m,alpha,w1,
                      w2,v1,v2, A2,A3,B2,B3,b,N,slope);
     Vx_t(ii,jj) = Vx_p(ii,jj) + V/2;
     Vz_p(ii,jj) = Vzfn_po(is(ii,jj),js(ii,jj), m,alpha,w1,
                      w2,v1,v2, A2,A3,B2,B3,b,N,slope);
     Vz_t(ii,jj) = Vz_p(ii,jj);
     else
     Vx_p(ii,jj) = Vxfn_po(is(ii,jj),zero, m,alpha,w1,
                       w2,v1,v2, A2,A3,B2,B3,b,N,slope);
     Vx_t(ii,jj) = Vx_p(ii,jj) + V/2;
     Vz_p(ii,jj) = Vzfn_po(is(ii,jj),zero, m,alpha,w1,
                       w2,v1,v2, A2,A3,B2,B3,b,N,slope);
     Vz_t(ii,jj) = Vz_p(ii,jj);
     end
     cf_or(ii,jj)= atan(Vz_t(ii,jj)/Vx_t(ii,jj))*180/pi;
     dProduct(ii,jj) = Vx_t(ii,jj)*VRx + Vz_t(ii,jj)*VRz;
     % cosBeta is the cosine of angle between vectors
     % Beta is the angle in degree
     % magnitude of velocity
     mag_of_v(ii,jj)= sqrt(Vx_t(ii,jj)^2 + Vz_t(ii,jj)^2);
     cosBeta(ii,jj) = dProduct(ii,jj)/( mag_of_v(ii,jj)* abVR);
     Beta(ii,jj) = acos(cosBeta(ii,jj))*180/pi;
      if cf_or(ii,jj) < VR_or   % ccw is defined to be positive
      Beta(ii,jj)= -Beta(ii,jj);
    end
end
end
maxBeta = max(max(Beta));
minBeta = min(min(Beta));
%---interval is the vector that determines the contour interval
interval=[minBeta,-10, -8,-6,-4,-2,-0.2,0.2,1,2,4,6,8,10,maxBeta];
```

```
[cc,hh]= contour(is,js,Beta,interval);clabel(cc,hh,interval);
hold on;
%---Plot the ramp----%
x = linspace(-L/28,L/28,30);
shapef = 0;
exag_factor = 1;
for kk = 1:1:N
   Bk = 2*2*h*(sin((2*kk-1)*(pi-W/2))+
             sin((2*kk-1)*W/2))/(W*pi*(2*kk-1)^2);
   rk = sin((2*kk-1)*pi/N)/((2*kk-1)*pi/N);
  A_pa=Bk*rk;
  shapef = shapef + exag_factor*A_pa*sin((2*kk-1)*x);
end
plot (x,shapef,'k');
axis equal;
%----plot the backlimb bisector (X')----%
zeta = (180-slope)/2;
xx1 = [-W/2 (-0.4*cos(zeta*pi/180)-W/2) ];
zz1 = [-h 0.4*sin(zeta*pi/180)-h];
line(xx1,zz1);
axis([-0.22,0.22,-h,0.4]);
```

APPENDIX H

SOURCE CODE FOR BACKLIMB TRISHEAR MODEL

```
V0 = 5;
alpha = -20*pi/180;  % asymmetry angle
phi = 20*pi/180;     % 2*phi is apical angle
theta = 20*pi/180;   % fault angle
lambta0 = alpha-theta/2;
lambta1 = alpha+theta/2;

deltaV0 = (V0*tan(theta)*tan(abs(theta/2
              -alpha)))/(1+tan(theta)*tan(abs(theta/2-alpha)));
V1 = (V0-deltaV0*sign(theta/2-alpha))/cos(theta);

V0x = V0*sin(abs(lambta0))*sign(lambta0);
V0y = -V0*cos(abs(lambta0));
V1x = V1*sin(abs(lambta1))*sign(lambta1);
V1y = -V1*cos(abs(lambta1));

[is,js] = meshgrid(1:1:21, -10:1:10);
C =(V1x-V0x)*(tan(phi)/4)+V0y;
for ii=1:21
  for jj=1:21
   if js(ii,jj) >= is(ii,jj)*tan(phi)
   Px(ii,jj)= V0x;
   Py(ii,jj)= V0y;
  elseif js(ii,jj)<= -is(ii,jj)*tan(phi)
    Px(ii,jj)= V1x;
    Py(ii,jj)= V1y;
  else
    xtemp = V0x/2*(js(ii,jj)/(is(ii,jj)*tan(phi))+1)
             -V1x/2*(js(ii,jj)/(is(ii,jj)*tan(phi))-1);
```

```
    Px(ii,jj)= xtemp;
    ytemp =(V0x-V1x)*(1/(4*tan(phi))*(js(ii,jj)/ is(ii,jj))^2)+C;
    Py(ii,jj)= ytemp;
  end
 end
end
%------ coordinate transformation-----%
X = cos(pi/2-lambta0)*Px-sin(pi/2-lambta0)*Py;
Y = sin(pi/2-lambta0)*Px+cos(pi/2-lambta0)*Py;
inew = cos(pi/2-lambta0)*is-sin(pi/2-lambta0)*js;
jnew = sin(pi/2-lambta0)*is+cos(pi/2-lambta0)*js;
%---plot the triangular boundaries----%
gamma1 = pi/2-phi+lambta0;  %inclination of trishear boundary
xx1 = [0 -25*cos(gamma1) ];
zz1 = [0 25*sin(gamma1)];
line(xx1,zz1);
hold on;
gamma2 = pi/2+phi+lambta0;
xx2 = [0 -25*cos(gamma2) ];
zz2 = [0 25*sin(gamma2)];
line(xx2,zz2);
%--- plot velocity field----%
quiver(inew, jnew, X,Y,0.6);
axis image;
hold on;
%---draw the fault, plot two lines----%
%---lower detachment---%
x1 = [-12 0];
y1 = [0 0];
line(x1,y1);
%---fault ramp----%
x2 = [0 20];
y2 = [0 20*tan(theta)];
line(x2,y2);
```

```
%----plot the trishear bisector-------%
zeta = (pi-theta)/2+alpha;
xx3 = [0 -22*cos(zeta) ];  % x-range of the bisector
zz3 = [0 22*sin(zeta)];   % z-range of backlimb bisector.
line(xx3,zz3);
%---Beta contour-----%
Vrx_prime = (V0x+V1x)/2;
Vry_prime = C;
%---coordinate transformation--get VR
VRx = cos(pi/2-lambta0)*Vrx_prime-sin(pi/2-lambta0)*Vry_prime;
VRy = sin(pi/2-lambta0)*Vrx_prime+cos(pi/2-lambta0)*Vry_prime;
abVR = sqrt(VRx^2 + VRy^2);
%The orientation of VR in angle, CCW from x-axis is positive
VR_or = atan(VRy/VRx)*180/pi;
for ii=1:21
  for jj=1:21
     % orientation of velocity vectors
     ca_or(ii,jj)=atan(Y(ii,jj)/X(ii,jj))*180/pi;
     dProduct(ii,jj) = X(ii,jj)*VRx + Y(ii,jj)*VRy;
     cos_Beta(ii,jj) = dProduct(ii,jj)/(sqrt(X(ii,jj)^2
                      + Y(ii,jj)^2) * abVR);
     Beta(ii,jj) = acos(cos_Beta(ii,jj))*180/pi;
     if ca_or(ii,jj) < VR_or
         Beta(ii,jj)= -Beta(ii,jj);
    end
  end
end
maxBeta = max(max(Beta));
minBeta = min(min(Beta));
%---cnumber is contour intervals
cnumber = [minBeta -8 -6 -4 -2 0  2  4  6  8  10];
[cc,hh] = contour(inew,jnew,Beta,cnumber);clabel(cc,hh,cnumber);
```

APPENDIX I

SOURCE CODE FOR TRISHEAR MODEL OF A FAULT-BEND FOLD

The following source code calculate the velocity field and plot β contour of the trishear model of a fault-bend fold. It assumes that a forelimb trishear zone locates at the upper ramp-flat corner of a fault-bend fold and interfere with the lower fault bend. The assumptions and velocity solution follow Cristallini and Allmendinger (2002) backlimb trishear model.

```
V0 = 5;
alpha = -20*pi/180;  % asymmetry angle
phi = 20*pi/180;     % 2*phi is apical angle
theta = 20*pi/180;   % fault angle
lambta0 = alpha-theta/2;
lambta1 = alpha+theta/2;

deltaV0 = (V0*tan(theta)*tan(abs(theta/2
              -alpha)))/(1+tan(theta)*tan(abs(theta/2-alpha)));
V1 = (V0-deltaV0*sign(theta/2-alpha))/cos(theta);
V0x_o = V0*sin(abs(lambta0))*sign(lambta0);
V0y_o = -V0*cos(abs(lambta0));
V1x_o = V1*sin(abs(lambta1))*sign(lambta1);
V1y_o = -V1*cos(abs(lambta1));
C1 = (V1x_o-V0x_o)*(tan(phi)/4)+V0y_o;
%--updated initial condition for lower trishear zone
V0x = V0x_o-V1x_o/2;
V0y = V0y_o-V1y_o/2;
V1x = V1x_o/2;
V1y = V1y_o/2;
C = (V1x-V0x)*(tan(phi)/4)+V0y;
%---velocity field at the lower fault bend---%
[is,js] = meshgrid(0:1:30, -15:1:15);
for ii = 1:31
```

```
  for jj = 1:31
   if js(ii,jj) >= is(ii,jj)*tan(phi)
   Px(ii,jj)= V0x;
   Py(ii,jj)= V0y;
  elseif js(ii,jj) <= -is(ii,jj)*tan(phi)
    Px(ii,jj)= V1x;
    Py(ii,jj)= V1y;
  else
    xtemp = V0x/2*(js(ii,jj)/(is(ii,jj)*tan(phi))+1)
             -V1x/2*(js(ii,jj)/(is(ii,jj)*tan(phi))-1);
    Px(ii,jj)= xtemp;
    ytemp =(V0x-V1x)*(1/(4*tan(phi))*(js(ii,jj)/ is(ii,jj))^2)+C;
    Py(ii,jj)= ytemp;
  end
 end
end
Px(16,1) = (V0x+V1x)/2;
Py(16,1) = C;
%---the two corners are shifted----%
if lambta0 <0
   eta = pi/2+theta-abs(lambta0);
else
   eta = pi/2-theta-abs(lambta0);
end
s_x=8;   % shift in x' direction
s_y_real=s_x/tan(eta);
s_y = round(abs(s_y_real));% shift in y' direction
zx=flipud(Px);
Pxt=Px;
Pxt(1:31-s_x,1+s_y:31)=Pxt(1:31-s_x,1+s_y:31)+zx(1+s_x:31,1:31-s_y);
Pxt(32-s_x:31,1+s_y:31)=V0x_o*ones(s_x,31-s_y);
Pxt(16:31,1:s_y)=V0x_o*ones(16,s_y);
Pxt(1:16-s_x,1:s_y)=zeros(16-s_x,s_y);
zy=flipud(Py);
```

```
Pyt=Py;
Pyt(1:31-s_x,1+s_y:31)=Pyt(1:31-s_x,1+s_y:31)+zy(1+s_x:31,1:31-s_y);
Pyt(32-s_x:31,1+s_y:31)=V0y_o*ones(s_x,31-s_y);
Pyt(16:31,1:s_y)=V0y_o*ones(16,s_y);
Pyt(1:16-s_x,1:s_y)=zeros(16-s_x,s_y);

%---Length of ramp------%
Length = sqrt(s_x^2+s_y^2);
%------ coordinate transformation-----%
X = cos(pi/2-lambta0)*Px-sin(pi/2-lambta0)*Py;
Y = sin(pi/2-lambta0)*Px+cos(pi/2-lambta0)*Py;
inew = cos(pi/2-lambta0)*is-sin(pi/2-lambta0)*js;
jnew = sin(pi/2-lambta0)*is+cos(pi/2-lambta0)*js;
%---plot the backlimb triangular boundaries----%
%gamma1 is the inclination of trishear boundary
gamma1 = pi/2-phi+lambta0;
xx1 = [0 -25*cos(gamma1) ];
zz1 = [0 25*sin(gamma1)];
line(xx1,zz1);
hold on;
gamma2 = pi/2+phi+lambta0;
xx2 = [0 -25*cos(gamma2) ];
zz2 = [0 25*sin(gamma2)];
line(xx2,zz2);
%--- plot velocity field----%
quiver(inew, jnew, X,Y,0.6);
axis image;
%---plot the forelimb triangular boundaries---%
W = Length*cos(theta);  % ramp width
H = Length*sin(theta);   % ramp height
%---trishear boundary of foreland trishear zone---%
xx3 = [0+W -25*cos(gamma1)+W ];
zz3 = [0+H 25*sin(gamma1)+H];
line(xx3,zz3);
```

```
xx4 = [0+W -25*cos(gamma2)+W ];
zz4 = [0+H 25*sin(gamma2)+H];
line(xx4,zz4);

%---draw the fault, plot two flats and one ramp------%
%---lower flat---%
x1 = [-12 0];
y1 = [0 0];
line(x1,y1);
%---fault ramp----%
x2 = [0 W];
y2 = [0 H];
line(x2,y2);
%---upper flat-----%
x3 = [W W+12];
y3 = [H H];
line(x3,y3);
%----plot the trishear bisector 1------%
zeta=(pi-theta)/2+alpha;
xx5 = [0 -25*cos(zeta) ];  % x-range of the bisector
zz5 = [0 25*sin(zeta)];   % z-range of backlimb bisector.
line(xx5,zz5);
%----plot the trishear bisector 2------%
zeta = (pi-theta)/2+alpha;
xx6 = [W -25*cos(zeta)+W ];
zz6 = [H 25*sin(zeta)+H];
line(xx6,zz6);
%---Beta contour-----%
Vrx_prime = (V0x_o+V1x_o)/2;
Vry_prime = C1;
%---coordinate transformation--get VR
VRx = cos(pi/2-lambta0)*Vrx_prime-sin(pi/2-lambta0)*Vry_prime;
VRy = sin(pi/2-lambta0)*Vrx_prime+cos(pi/2-lambta0)*Vry_prime;
abVR = sqrt(VRx^2 + VRy^2);
```

```
%The orientation of VR in angle, CCW from x-axis is positive
VR_or = atan(VRy/VRx)*180/pi;
for ii = 1:31
  for jj = 1:31
     % orientation of velocity vectors
     ca_or(ii,jj)=atan(Y(ii,jj)/X(ii,jj))*180/pi;
     dProduct(ii,jj) = X(ii,jj)*VRx + Y(ii,jj)*VRy;
     cos_Beta(ii,jj) = dProduct(ii,jj)/(sqrt(X(ii,jj)^2
                     + Y(ii,jj)^2) * abVR);
     Beta(ii,jj) = acos(cos_Beta(ii,jj))*180/pi;
     if ca_or(ii,jj) < VR_or
         Beta(ii,jj)= -Beta(ii,jj);
    end
  end
end
maxBeta = max(max(Beta));
minBeta = min(min(Beta));
%---cnumber is contour intervals
cnumber = [minBeta -8 -6 -4 -2 0  2  4  6  8  10];
[cc,hh] = contour(inew,jnew,Beta,cnumber);clabel(cc,hh,cnumber);
```

VITA

Name: Li Zhang

Education:

M.S., August 2003, Texas A&M University, Department of Geology&Geophysics. Thesis: Folds above angular fault bends: mechanical constraints for backlimb trishear kinematic models. Major Geology.

M.S., July 2000, Southwest Petroleum Institute, Department of Geology. P.R. China. Thesis: Structural analysis on a complex structure at Piyaman, Tarim basin. Major Geology.

B.E., July 1997, Southwest Petroleum Institute, Department of Geology. P.R. China. Major Exploration Geophysics.

Permanent Address:

Department of Geology&Geophysics

Texas A&M University

College Station, TX 77843

USA